Geochemical and microstructural evidence for interseismic changes in fault zone permeability and strength, Alpine Fault, New Zealand

Carolyn Boulton[1,2], Catriona D. Menzies[3], Virginia G. Toy[4], John Townend[5], and Rupert Sutherland[6,5]

[1]Department of Geological Sciences, University of Canterbury, Christchurch, New Zealand

[2]School of Environmental Sciences, University of Liverpool, Liverpool, United Kingdom

[3]Ocean and Earth Science, National Oceanography Centre Southampton, University of Southampton, Southampton, United Kingdom

[4]Department of Geology, University of Otago, Dunedin, New Zealand

[5]School of Geography, Environmental, and Earth Sciences, Victoria University of Wellington, Wellington, New Zealand

[6]GNS Science, Lower Hutt, New Zealand

Abstract

Oblique dextral motion on the central Alpine Fault in the last c. 5 Myr has exhumed garnet-oligoclase facies mylonitic fault rocks from c. 35 km depth. During exhumation, deformation, accompanied by fluid infiltration, has generated complex lithological variations in fault-related rocks retrieved during Deep Fault Drilling Project (DFDP-1) drilling at Gaunt Creek, South Island, New Zealand. Lithological, geochemical, and mineralogical results reveal that the fault comprises a core of highly comminuted cataclasites and fault gouges bounded by a damage zone containing cataclasites, protocataclasites, and fractured mylonites. The fault core-alteration zone extends c. 20-30 m from the principal slip zone (PSZ) and is characterized by alteration of primary phases to phyllosilicate minerals. Alteration associated with distinct mineral phases occurred proximal the brittle-to-plastic transition ($T \leq 300$-400°C, 6-10 km depth) and at shallow depths (T=20-150°C, 0-3 km depth). Within the fault core-alteration zone, fractures have been sealed by authigenic precipitation of calcite and phyllosilicates. This sealing has decreased fault normal permeability and increased rock mass competency, potentially promoting interseismic strain buildup. **Keywords:** *Alpine*

Fault, New Zealand, fault rocks, alteration, mineralogy, geochemistry, microstructure, permeability, sealing, seismic cycle.

Highlights:

- The mineralogy of fault rocks recovered in DFDP-1 is consistent for >120 km along-strike
- Authigenic phyllosilicates and carbonates occur in the Alpine Fault core
- Alpine Fault core alteration reactions alter fault zone permeability and promote interseismic strain buildup

1 Introduction

The Alpine Fault of New Zealand ruptures quasi-periodically in large magnitude (*Mw* ~ 8) earthquakes [*Berryman et al.*, 2012], and it represents the largest onshore seismic hazard in the country of 4.4 million people. Earthquakes are frictional instabilities, and their nucleation, propagation, and arrest is governed by fault zone properties [e.g., *Sibson*, 1977, 1982, 1992; *King*, 1986; *Wesnousky*, 1988; *Scholz*, 2002; *Ben-Zion*, 2008]. A fault zone commonly contains a fault core, often containing at least one principal slip zone (PSZ), of fine-grained granular materials (gouge, cataclasite, or pseudotachylyte) where most coseismic displacement occurs [*Caine et al.*, 1996; *Chester and Chester*, 1998; *Sibson*, 2003]. Within the fault core, gouges, cataclasites and breccias are interpreted to result from particle size reduction by fragmentation, abrasion, and/or comminution accompanied by translation and rotation [e.g., *Sibson*, 1977; *Chester and Logan*, 1986; *Chester and Chester*, 1998]. Fault cores are commonly flanked by damage zones, rock bodies with micro- to macro-scale fractures that form

as a result of off-fault deformation and fluid-rock interactions [e.g., *Chester and Logan*, 1986; *Caine et al.*, 1996].

Characterizing three-dimensional variations in fault zone properties, and taking into account time-dependent changes in these properties, is essential to understanding the physical processes that drive seismicity. As the last Alpine Fault earthquake occurred in 1717 CE and the average recurrence interval is 329±68 years, current observations of the fault are ideally timed to document its late interseismic physicochemical properties [e.g., *Wells and Goff*, 2007; *Sutherland et al.*, 2007; *Howarth et al.*, 2012; *Berryman et al.*, 2012; *Townend et al.*, 2009, 2013]. The first phase of Deep Fault Drilling Project (DFDP-1) drilling in January-February 2011 retrieved a full sequence of Alpine Fault hanging wall, fault core, and footwall fault rocks, enabling detailed examination of fault zone elements on the 0.01-100 m scale [*Sutherland et al.*, 2012; *Townend et al.*, 2013; *Toy et al.*, 2015]. This study presents new field, drilling, and laboratory data on the lithology, mineralogy, and major element geochemistry of the Alpine Fault at Gaunt Creek.

2 Geological Setting

2.1 Tectonic history

The New Zealand continental landmass, Zealandia, underwent multiple phases of tectonic deformation as part of the Gondwana supercontinent [*Landis and Coombs*, 1967; *Carter and Norris*, 1976; *Mortimer*, 2004]. Zealandia was rifted during the Late Cretaceous and finally broke away from Australia and Antarctica landmass by c. 80 Ma, with subsequent opening of the South Pacific and Tasman Sea [*Molnar et al.*, 1975; *Gaina et al.*, 1998; *Sutherland*, 1999]. At c. 45 Ma (Eocene), a new plate boundary propagated through Zealandia [*Sutherland*, 1995]. Strike-slip motion began on the

proto-Alpine Fault c. 30 Ma [*Sutherland et al.*, 2000; *Lamb et al.*, 2015, 2016], and present day oblique convergence along the Alpine Fault initiated c. 8-5 Ma as a result of a subtle shift in the location of the instantaneous Euler pole for Australian-Pacific plate motion [*Walcott*, 1984; *Batt et al.*, 2004; *Cande and Stock*, 2004].

2.2 Regional structure

The Alpine Fault is a crustal-scale transpressive fault that links Pacific Plate subduction in the north (Hikurangi margin) to Australian Plate subduction in the south (Puyseguer margin) (Figure 1). The Alpine Fault has accommodated >460 km of cumulative displacement [*Wellman*, 1953; *Lamb et al.*, 2016]. The focus of this study is the Alpine Fault at Gaunt Creek, a tributary of the Waitangi-taona River on the central section of the Alpine Fault that extends for 250 km from the Toaroha River to the Martyr River. Along the central section, the fault has a strike-slip rate of 27-29 mm/yr and a dip-slip rate of 2-8 mm/yr [*Simpson et al.*, 1994; *Cooper and Norris*, 1994; *Barth et al.*, 2013]. In the near surface (<2 km depth), the central Alpine Fault exhibits sequences of north-northeast striking oblique thrust faults and linking east-northeast striking dextral faults, but at depth the orientation of the Alpine Fault parallels the foliation of exhumed mylonites and ultramylonites (055º/45ºSE) [*Norris and Cooper*, 2007; *Barth et al.*, 2012]. The structure of the central section differs markedly from the steeply dipping oblique-normal southern Alpine Fault [see also *Berryman et al.*, 1992; *Barth et al.*, 2013] (Figure 1).

2.3 Gaunt Creek structure

At Gaunt Creek, there are two natural exposures of the Alpine Fault basal thrust, defined by *Norris and Cooper* [2007] as the de facto plate boundary oblique thrust contact between hanging wall Pacific plate cataclasites and footwall Australian plate

gravels, intrusives, or metasediments (Figure 2). One natural exposure occurs in a well-studied scarp on the south side of Gaunt Creek [*Cooper and Norris,* 1994; *Boulton et al.,* 2012], and the other is a terrace on the north side of Gaunt Creek [*De Pascale and Langridge,* 2012; *Boulton et al.,* 2012] (Figures 2 and 3). Hanging wall cataclasites and mylonites derived from metabasic and quartzofeldspathic schist protoliths outcrop in both localities [e.g., *Cooper and Norris,* 1994]. The basal thrust at Gaunt Creek has changed from a moderately southeast-dipping, oblique reverse fault to a shallowly dipping thrust that has accommodated over 180 m of overthrusting [*Cooper and Norris,* 1994]. The basal thrust exposed in the scarp on the south side of Gaunt Creek has a mean orientation of 059º/42ºSE with mean slickenline striations oriented 24/086. The fault plane exposed in the terrace on the north side of Gaunt Creek is more shallowly dipping, with an average orientation of 005º/28ºSE (Figure 2). No slickenline striations were found along the contact between the terrace fault gouge and footwall gravel contact. Drillcore retrieved during DFDP-1A and 1B was not oriented, and estimates of fault dip based on basal gouge contacts have an estimated margin of error of ±5°. The fault plane in DFDP-1A dips approximately 25-35°, and the primary fault plane in DFDP-1B dips approximately 45-55° (see also Figure 2 caption) [*Sutherland et al.,* 2012].

3 Methods

3.1 Drilling operation

In Phase 1 of drilling, January and February 2011, the DFDP project completed two vertical boreholes at Gaunt Creek. DFDP-1A drilled to 100.6 m depth and DFDP-1B drilled to 151.4 m depth [*Sutherland et al.,* 2012] (Figure 3). Hanging wall, fault core, and footwall sections of fault-related rocks were recovered, wireline logs were

completed, hydraulic observations were made, and downhole observatories for the long-term monitoring of temperatures, fluid pressures, and seismicity were established. Drilling methods are described elsewhere in the detailed operational report [*Sutherland et al.*, 2011].

3.2 Core logging

Detailed core logs were made of 148 m of near-complete whole-rock cores (PQ, 85 mm- diameter). Initial geological logs completed on site recorded lithology, color, distribution, styles and orientations of meso- to micro-scale structures. More detailed imaging, logging, and lithological descriptions of the core was conducted after transport to the University of Otago [for core-logging methods, see *Sutherland et al.*, 2011].

3.3 Thin section preparation

Representative samples of fault-related rocks were selected and made into petrographic thin sections. Petrographic thin sections of fragile fault gouges and cataclasites were prepared dry and polished using 1 μm diamond paste. Less friable drillcore materials were prepared using standard petrographic thin section making techniques.

3.4 Analytical methods

Qualitative X-ray diffraction (XRD) analyses were conducted on thirty-four clean samples collected from DFDP-1A and DFDP-1B drillcore. Qualitative XRD measurements were performed on a PANalytical X'Pert PRO MPD PW 3040/60 X-ray diffractometer in the Department of Geology, University of Otago. Measurement conditions were 40 kV, 30 mA, CuK_{α} radiation with 0.125° divergence slit size. XRD

patterns were recorded in steps of 0.0080 °2θ using X'Pert Data Collector version 2.0e and processed with X'Pert HighScore version 2.2b.

Quantitative XRD analyses were conducted on six fault gouges and cataclasites in DFDP-1B at CSIRO Land and Water, Urrbrae, Austrlia. XRD patterns were recorded in steps of 0.017 °2θ on a PANalytical X'Pert Pro Multipurpose Diffractometer using Fe-filtered Co Kα radiation, variable divergence slit, 1° antiscatter slit and fast X'Celerator Si strip detector. Quantitative analysis was performed using SIROQUANT, a commercially available software package from Sietronics Pty Ltd. To document along-strike variations in the mineralogy of principal slip zone gouges and cataclasites, seventeen additional quantitative whole rock XRD analyses were conducted on surface-outcrop fault gouges and cataclasites collected from localities pictured in Figure 1.

A subset of DFDP-1 samples, together with fault core samples from natural exposures at Gaunt Creek, were analysed for major element geochemistry using Inductively Coupled Plasma Atomic Emission Spectroscopy (ICP-AES) and X-ray fluorescence (XRF) techniques. Thirty-nine clean samples from DFDP-1A and DFDP-1B, weighing between 10 g and 30 g, were selected for ICP-AES analysis by ALS Minerals, ALS Canada Ltd., North Vancouver, British Columbia, Canada. Major element oxide analysis of six DFDP-1A samples was performed using XRF at the Department of Geology, University of Otago, using a Philips PW2400 X-ray fluorescence spectrometer.

To determine loss on ignition (LOI), 1.0 g of prepared sample was placed in an oven at 1000 °C for 1 hour, cooled, and then re-weighed by ALS Minerals. At the Department of Geology, University of Otago, 2.0 g of rock powder was placed in an

oven at 1100 °C for 2 hours, cooled, and then re-weighed. The percentage loss on ignition is reported as the percentage difference in sample weight.

To constrain the along-strike applicability of DFDP-1 results, twenty-three additional major element analyses were conducted on ultramylonite (1), hanging wall cataclasites (8), fault core gouges (12), and footwall gravel cataclasites (2) using a combination of the above methods. Sample collection localities span 234 km along-strike of the Alpine Fault and are indicated in Figure 1. A detailed analysis of along-strike variations in fault gouge, cataclasite, and footwall gravel major element geochemistry is outside the scope of this research, and the following results, discussion, and conclusions sections focus on DFDP-1 samples. Tabulated results for other localities along strike can be found in supplementary material along with reports on analytical error and detailed qualitative and quantitative XRD, ICP-AES, and XRF methods (see also Table 4 caption) (Supplements S1-S3).**4 Results**

4.1 Fault zone structure

Four main fault-rock units were initially identified in the DFDP-1 boreholes: hanging wall ultramylonite, hanging wall cataclasite, principal slip zone fault gouge (PSZ), and footwall cataclasite [*Sutherland et al.*, 2012]. Within DFDP-1B, two PSZ gouges were identified: one between hanging wall cataclasite and the footwall cataclasite (PSZ-1), and another within footwall cataclasites (PSZ-2) (Figure 3). Within 50 m of the PSZ, clay-filled zones were identified, and enhanced calcite and phyllosilicate mineralization was found within c. 20 m of the PSZ [*Sutherland et al.*, 2012]. The PSZ fault gouge that marks the boundary between hanging wall cataclasites and footwall gravel was intercepted at 90.5 m depth in DFDP-1A. The PSZ-1 fault gouge that marks the boundary between hanging wall cataclasites and footwall

granitoid or metasediment-derived cataclasites was intercepted at 128.3 m in DFDP-1B (DFDP-1B depths given here are corrected by +0.20 m following *Townend et al.* [2013]). Permeability decreases through the cataclasites and reaches a minimum at the PSZ fault gouges, but hanging wall mylonites are highly permeable [*Sutherland et al.*, 2012; *Carpenter et al.*, 2014].

4.2 Lithologic units

Using detailed imaging, core logging, lithological descriptions, and thin section analysis, a refined model of hanging wall, fault core, and footwall lithologic units has been developed [*Toy et al.*, 2012; *Townend et al.*, 2013; *Toy et al.*, 2015] (Figure 3) (Table 1). Fault rocks were described following the scheme proposed by *Sibson* [1977] and modified to include the presence of foliated cataclasites with an interconnected network of phyllosilicate minerals [*Chester et al.*, 1993; *Holdsworth*, 2004; *Jefferies et al.*, 2006]. Summaries of these lithologic units have been modified from *Toy et al.* [2015] and are outlined in Table 1.

Core-scale examples of each lithologic unit are given in Figure 3. Details are given in the caption. Figure 4 depicts plane-polarized optical microscopy (OM) images of the Units 2-3 transition (Figure 4a), Unit 4 (Figures 4b-d), Unit 5 (Figure 4g), Unit 6 (Figures 4e-f), and Unit 7 (Figure 4h). In Figures 5 and 6, scanning-electron microscope backscattered electron (BSE) images reveal the finer-scale details of compositional variations and microstructural features in lithologic units: 2 (Figures 5a-b); 3 (Figures 5c-d); 4 (Figures 5e-f); 5 (Figures 6a-d); 6 (Figures 5h and 6e-g); and 7 (Figure 6h).

4.3 Mineralogy

X-ray diffraction analyses provide an indication of the minerals present in abundances greater than c. 5%. All the samples analyzed contain quartz, plagioclase, white mica (muscovite and/or illite) and chlorite (clinochlore). Carbonate minerals (calcite + ankerite) are most prevalent in hanging wall samples (Units 1–5) and are only sporadically present in Units 6 and 7 beneath the 128.3 – 128.5 m PSZ in DFDP-1B. Potassium feldspar (K-feldspar) is only found in the hanging wall within 5 m of the PSZ in DFDP-1A and, primarily, beneath PSZ-1 in DFDP-1B (Table 2).

Six whole-rock samples from the DFDP-1B principal slip zone intervals (PSZ-1 and PSZ-2) were analysed for quantitative XRD analysis. The modal abundance of phyllosilicates in Units 5 (PSZ-1, 128.3 m; PSZ-2, 144.02 m; PSZ-2, 144.14 m depth), Unit 6 (143.9 m depth), and Unit 7 (144.28 m depth) does not vary significantly, being 35-36% for Units 5 and 6, and 27% for Unit 7. The primary difference between the samples lies in the presence of dioctahedral smectite (montmorillonite) in the Unit 5 brown gouges (Table 3).

Whereas nonfoliated and foliated cataclasites in the hanging wall and footwall contain the phyllosilicates chlorite and white mica, Unit 5 fault core gouges in the DFDP-1 boreholes contain kaolinite, dioctahedral smectite (montmorillonite), white mica, and rare chlorite (Tables 1-3). Standard X-ray diffraction techniques are unable to distinguish the white micas muscovite and illite, but the distinction is important because illite is a low-temperature authigenic phyllosilicate indicative of retrograde alteration concomitant with exhumation. Clay mineral polytype analyses on DFDP-1B clay separates recently revealed that high proportions of $1M_d$ authigenic illite (80-95%) occur only within the PSZ gouges [*Schleicher et al.*, 2015]. These results suggest that additional alteration reactions resulting in the formation of low temperature phyllosilicates are occurring preferentially in the Unit 5 gouges.

Montmorillonite-bearing Unit 5 gouges were also found on basal thrusts on a tributary of Little Man River, Waikukupa River, and Robinson Creek, an along-strike distance of 120 km on the central Alpine Fault (Figure 1) (Table 4). On the southern Alpine Fault, PSZ gouges contain saponite and serpentine and have been derived partly from ultramafic protoliths (Figure 1) (Table 4) [*Barth et al.*, 2013].

4.4 Major element geochemistry

Major element geochemistry and LOI results for DFDP-1A fault rocks are presented in Table 5; results for DFDP-1B fault rocks are presented in Table 6. The DFDP-1A borehole sampled hanging wall fault rocks, a single PSZ, and footwall gravels. DFDP-1B borehole samples span the hanging wall and footwall and include two PSZ intervals (Figure 3). Major element data show a clear distinction between the SiO_2, Al_2O_3, CaO, and K_2O contents of the Units 2-4 and Unit 6 fault rocks; Unit 5 gouges are distinguished by high CaO and LOI values (Figures 7 and 8). SiO_2 concentrations in hanging wall and footwall rocks overlap, but Unit 6 lower cataclasites between 128.04 and 128.22 m depth, and at 131.68 m depth, have the highest SiO_2 contents (70.70 – 74.60 wt.%) (Figure 8). Unit 6 lower cataclasites between 138.17 and 141.07 m also contain relatively higher amounts of Al_2O_3 (16.65 – 18.10 wt.%) (Figure 8).

In DFDP-1A, the highest CaO concentrations occur in the Unit 4 upper foliated cataclasite (90.32 m depth) and Unit 5 gouge (90.62 m depth) (14.75 and 6.83 wt.%, respectively) (Figure 7). In DFDP-1B, all Unit 3-5 fault rocks, with the exception of a Unit 5 gouge at 144.15 m depth, have higher CaO concentrations (2.79-6.72 wt.%) than the Unit 6 lower cataclasites (0.58-2.58 wt.%). The Unit 8 footwall gravel in DFDP-1A (91.3 m depth) records the lowest CaO content (1.36 wt.%). Overall, Unit 6 lower

cataclasites have mean higher K_2O (4.28±1.14 wt.%, n=13) concentrations than other footwall and hanging wall units (3.19±0.57 wt.%, n=26) (Figures 7 and 8). Na_2O shows less discernible trends but usually occurs more abundantly in the Unit 6 lower cataclasites (Figure 8).

All Unit 5 gouges, the Unit 4 foliated cataclasite at 90.32 m depth in DFDP-1A, and the Unit 3 upper unfoliated cataclasite at 116.72 m depth in DFDP-1B have elevated MnO contents (0.11-0.24 wt.%), particularly when compared to the Unit 6 cataclasites (0.01-0.08 wt.%) (Figures 7 and 8). Unit 6 lower cataclasites immediately below PSZ-1 contain relatively less Fe_2O_3 and MgO (1.31-2.92 wt.% and 0.59-1.39 wt.%, respectively), but considerable scatter exists within the hanging wall and footwall units. The Unit 7 breccia at 146.25 m depth has the highest concentration of P_2O_5 (0.44 wt.%) (Figure 8; see also Figure 4h). In both DFDP-1A and DFDP-1B, the Unit 5 gouges and adjacent Unit 4 upper foliated cataclasites have high LOI and CaO values (Figures 7 and 8).

Major element oxide data are presented on two ternary plots in Figure 9. Together with Pacific Plate quartzofeldspathic schist and metabasite, the Australian Plate Karamea Suite and Greenland Group protoliths define a trend line along which the majority of DFDP-1 hanging wall and footwall fault rocks lie (Figure 9A). The Unit 7 breccia lies at the $MgO+Fe_2O_3$ axis of the footwall trend line in both ternary plots (Figure 9). Unit 6 lower cataclasites have higher K_2O, Na_2O and Al_2O_3 compared with the other units and trend towards the average Karamea Suite protolith composition (Figure 9A). A trend towards higher CaO is exhibited by Unit 4 upper foliated cataclasites and Unit 5 gouges, with the DFDP-1B PSZ-2 gouge (144.15 m depth) having lower CaO than the DFDP-1B PSZ-1 gouge and DFDP-1A PSZ gouge (Figure 9B).

5 Discussion

5.1 Alteration zone processes

During exhumation from c. 35 km depth, brittle deformation of Alpine Fault mylonites, accompanied by fluid infiltration, has resulted in complex mineralogical and lithological variations in fault rocks retrieved during DFDP-1 drilling at Gaunt Creek. Results documented herein and referred to in publications by *Sutherland et al.* [2012], *Townend et al.* [2013], and *Toy et al.* [2015] reveal that the fault comprises a fault core of protocataclasites, cataclasites, and fault gouges bounded by a damage zone containing fractured ultramylonites (Figure 3). These results are consistent with previous descriptions of Alpine Fault rocks [e.g., *Reed*, 1964; *Sibson et al.*, 1979; *Norris and Cooper*, 2007; *Toy et al.*, 2008]. In the DFDP-1 drillcore, the fault core-alteration zone extends from the Unit 5 PSZ gouges c. 20-30 m into the hanging wall by using the first documented occurrence of retrogressed mineral assemblages in the Unit 2 brown–green–black ultramylonites to represent the maximum width of alteration zone processes [e.g., *Caine et al.*, 1996; *Sutherland et al.*, 2012]. Measurements made from fault rocks collected elsewhere on the central and southern Alpine Fault reveal that fault core mineralogy at the site of DFDP-1, Gaunt Creek, is similar to outcrops exposed for at least 120 km along-strike (Figure 1) (Tables 3, 4). We combine our observations with the temperature constraints of *Warr and Cox* [2001] and *Toy et al.* [2010] and the reactions documented by *Chamberlain et al.* [1999] and *Wintsch and Yeh* [2013] to suggest that at least two stages of chemical alteration have occurred in the Alpine Fault core-alteration zone (Figure 10). At temperatures at or near the brittle-to-ductile transition (T≤300-400°C), metasomatic alteration reactions resulted in albite or, potentially, K-feldspar replacement by muscovite, and biotite (phlogopite) replacement by chlorite (clinochlore). Hydrous chloritization of epidote and hornblende (actinolite)

316 may have also occurred (Figure 4c-d, 5e). Given its ubiquitous presence in alteration
317 zone lithological units including ultramylonites (Figure 5a), chlorite likely precipitated
318 at a range of temperatures less than 400°C, temperature conditions slightly broader than
319 those defined by Warr and Cox [2001] using microchemical data [see also *Vry et al.*,
320 2001]. At lower temperatures (T≤120°C), alteration reactions occurred in the presence
321 or absence of free electrons. That is, depending on local redox conditions, primary
322 minerals were altered to kaolinite, smectite (montmorillonite) and/or pyrite or smectite
323 (montmorillonite), kaolinite, Fe-hydroxide (goethite) and/or carbonate (Tables 3 and 4)
324 (Figures 4g, 6a-b, and 10).

325 For the standard metasomatic alteration reactions involving K-feldspar,
326 plagioclase, muscovite, biotite (phlogopite), and chlorite (clinochlore), volume loss or
327 gain, and corresponding variations in porosity and permeability, are governed by
328 fluid:rock ratios and Mg^{2+}/H^{+}, K^{+}/H^{+}, and Na^{+}/H^{+} activity ratios [*Wintsch et al.*, 1995;
329 *Wintsch and Yeh*, 2013]. Hydrolysis reactions involving the reactants K-feldspar,
330 muscovite, biotite (phlogopite), muscovite, chlorite (clinochlore), and albite usually
331 result in volume loss. Notably, however, a volume gain occurs during the alteration of
332 clinochlore to montmorillonite and during the alteration of muscovite to illite.
333 Precipitation of calcite and goethite also results in a volume gain of 36.9 cm^3 per mol
334 of calcite precipitated and 21.5 cm^3 per mol of goethite precipitated (Table 7). More
335 detailed microstructural observations are needed to document the reaction sequences
336 and their associated microstructures.

337 Although volume loss is commonly observed in fault cores, Alpine Fault rocks
338 gained volume wherever calcite, illite, montmorillonite, and/or goethite precipitated
339 (Figures 4 and 5) (Table 7) [e.g, *Goddard and Evans*, 1995; *Evans and Chester*, 1995;
340 *Schleicher et al.*, 2009; *Chen et al.*, 2013; see also *Isaacs et al.*, 2008]. On the Alpine

Fault, solid volume gain from the precipitation of authigenic clay minerals and calcite from circulating hydrothermal fluids would act to decrease fault rock permeability with time (see Section 5.5). Abundant evidence exists for the presence of vigorous hydrothermal system and advective fluid flow at depth east of the Alpine Fault beneath the Southern Alps [*Craw*, 1988; *Koons and Craw*, 1991; *Allis and Shi*, 1995; *Koons et al.*, 1998; *Menzies et al.*, 2016]. Multiple factors drive the Southern Alps hydrothermal system, including elevated isotherms, steep topography, abundant rainfall [*Barnes et al.*, 1978; *Koons*, 1987; *Koons and Craw*, 1991; *Menzies et al.*, 2014, 2016], production of overpressured metamorphic fluids at depth [*Craw and Campbell*, 2004; *Vry et al.*, 2001, 2009], and perhaps coseismic increases in fault rock permeability accompanied by overpressured metamorphic fluid migration [*Sibson*, 1992; *Townend et al.*, 2013]. Within this system, rising rock-exchanged and mantle-derived fluids mix with descending meteoric waters and emerge in the fault's hanging wall as warm springs [*Barnes et al.*, 1978; *Jenkin et al.*, 1994; *Templeton et al.*, 1998; *Upton et al.*, 1995, 2000, 2002; *Menzies et al.*, 2014, 2016] (Figure 11).

5.2 Major element geochemistry variations

Major element geochemistry results presented in Figures 7, 8, and 9 have not been normalized to account for changes in relative element abundance based on silica mobility in the fault zone [e.g., *Gresens*, 1967; *Grant*, 1986]. TiO_2 is commonly assumed to be immobile in fault zones [e.g., *Schleicher et al.*, 2009], but normalizing major element oxides to TiO_2 requires assuming a value for a single unaltered protolith. Moreover, neometamorphic titanite that postdates chloritization of Alpine Fault mylonites at high temperatures (c.425-500 ºC) has been identified [*Vry et al.*, 2001]. Nevertheless, the major element data reveal trends within the DFDP-1 lithologic units. The Unit 5 gouges have lower SiO_2, higher CaO concentrations, and anomalously high

366 LOI values when compared to adjacent hanging wall and footwall lithologic units
367 (Figures 7 and 8). These measurements corroborate our petrographic and XRD
368 identification of retrograde clay minerals (illite and montmorillonite) and calcite
369 cement in the PSZ gouges (Table 3) (Figures 6a-b and 6d).

370 The DFDP-1A Unit 5 gouge at 90.62 m and the DFDP-1B Unit 6 lower
371 cataclasites have higher K_2O contents than background hanging wall material (Figures
372 7 and 8). The Unit 6 lower cataclasites were derived in part from granitoid protoliths
373 rich in quartz, plagioclase, and K-feldspar, and thus reflect the chemistry of these
374 minerals (the Australian Plate Karamea Suite) (cf. Figures 4e, 5e and 9). The presence
375 of elevated K_2O in the DFDP-1A PSZ gouges provides evidence for incorporation of
376 footwall K-feldspar, adularia, and/or potassic pseudotachylyte, which is common
377 within cataclasites at Gaunt Creek [*Norris and Cooper*, 2007; *Toy et al.*, 2011]. In
378 addition, the major element geochemistry K_2O data are supported by XRD and/or thin
379 section observations of K-feldspar in this unit and in the Unit 4 upper foliated gouges
380 up to 5 m from the PSZ (Table 2) (Figures 4b and 5a-b).

381 Further trace element and isotopic investigations are required to determine the
382 origin of the Unit 7 breccia. Despite being the lowest structural unit in the boreholes,
383 the Unit 7 breccia shares the same mineral assemblage as both the upper (Unit 3 and
384 Unit 4) and lower (Unit 6) catalcasites (quartz + potassium feldspar + plagioclase +
385 biotite + chlorite + muscovite ± epidote + accessory minerals) (Tables 1 and 2). In thin-
386 section, Unit 7 contains visibly more graphite and apatite than the other lithologic units,
387 the latter being reflected in elevated P_2O_5 concentrations (Table 6) (Figures 4h and 8).
388 However, the two Unit 7 samples lie at the intersection of the hanging wall and footwall
389 trends in Figure 9.

390 The major element geochemistry of fault rocks retrieved from the DFDP
391 drillholes and collected from nearby natural exposures generally reflects the
392 composition of the metamorphic or plutonic protoliths [*Roser and Cooper*, 1990; *Roser*
393 *and Korsch*, 1999; *McClintock and Cooper*, 2003; *Pitcairn et al.*, 2006] (Figure 9).
394 Because fault rocks within the fault core and damage zone are derived from multiple
395 protoliths and have experienced multiple phases of deformation, including exhumation
396 and dextral translation along the Alpine Fault [*Little et al.*, 2005; *Cooper and Norris*,
397 2011], it is difficult to ascertain the original composition of the fault rocks, the nature
398 of fluid mobility through time, and the amount of mass gained and lost [e.g., *O'Hara*,
399 1988; *Ague*, 1994; *Evans and Chester*, 1995] (Tables 5 and 6) (Figure 9). In order to
400 asses original rock protolith compositions and constrain geochemical variability due to
401 fluid-rock interactions – thus resulting in estimates for mass loss and mass gain in the
402 fault zone – further research involving immobile trace elements and radiogenic isotopes
403 is required.

404 **5.3 Effect of alteration reactions on fault zone rheology**

405 Marking the transition from the damage zone to alteration zone, Unit 1 and 2
406 ultramylonites exhibit microstructures indicative of deformation by dislocation creep;
407 a retrogressed mineral assemblage in Unit 2 indicates some alteration took place in this
408 lithologic unit [e.g., *Prior*, 1988; *Norris and Cooper*, 2003, 2007; *Toy et al.*, 2008,
409 2015] (Figure 3). Within the alteration zone, brittle deformation involving cataclasis
410 has formed Unit 3 upper unfoliated cataclasites, some of which show evidence of
411 sealing via multiple generations of carbonates, which are comparatively sparse in the
412 Alpine Fault mylonite sequence [A. Cooper, *pers. comm.*, 2012] (Figures 5c, 7 and 8).
413 Shear deformation of comminuted and precipitated phyllosilicate minerals, particularly
414 chlorite and white mica, has also resulted in the formation of networks of anastomosing

phyllosilicates (Unit 4 upper foliated cataclasites) (Figures 4c-d and 5g). However, in the Unit 5 fault gouges, these foliations have been disrupted by cataclasis. Furthermore, chlorite and potassium feldspar have altered to montmorillonite in these gouges; potassium feldspar and/or albite have also reacted to form kaolinite (Tables 3 and 4) (e.g., Figures 6a-d).

Alpine Fault mineralogical and structural variations have rheological implications best understood in the context of similar natural and analog fault rocks. Fault cores containing gouges (or ultracataclasite) bounded by foliated cataclasites have been described from many inactive fault zones, including the Geesaman fault zone, Arizona, USA, exhumed from <13 km depth [*Janecke and Evans*, 1988; *Schulz and Evans*, 1998, 2000], the Punchbowl Fault, California, USA, exhumed from 2-4 km depth [*Chester et al.*, 1993], the Median Tectonic Line, Japan, exhumed from 5-10 km depth [*Jefferies et al.*, 2006], and the Zuccale Fault, exhumed from <8 km depth [*Collettini and Holdsworth*, 2004]. Within these fault cores, the brecciation and/or cataclasis of fault zone protolith(s) created fluid migration pathways, triggering phyllosilicate mineralization via fluid-assisted hydration reactions [e.g., *Janecke and Evans*, 1998]. When phyllosilicate minerals form an interconnected fabric with a preferred orientation of (001) parallel to the shearing direction, frictional sliding can occur at low resolved shear stresses because of weak (001) interlayer bond strengths and/or adsorbed water films [e.g., *Moore and Lockner*, 2004; *Collettini et al.*, 2009; *Tembe et al.*, 2010].

At higher temperatures and pressures, at depths of 3 to 15 km that encompass the brittle-to-plastic transition, strain-rate and grain-size dependent diffusion-assisted pressure solution creep (also termed “grain size sensitive creep”) may operate in foliated fault rocks [e.g., *Sibson*, 1977; *Chester and Higgs*, 1992; *Hickman et al.*, 1995;

440 *Bos and Spiers*, 2002]. Microphysical models of this mechanism predict the shear
441 strength of foliated fault rocks, such as the Unit 4 foliated cataclasites, is governed by:
442 resistance to shear along phyllosilicate foliations; solution transfer in rigid mineral
443 grains; or dilation as sliding foliae are forced to overcome geometrical incompatibilities
444 [*Bos and Spiers*, 2002]. Analog experiments conducted to high-strain have shown that
445 the development of a through-going phyllosilicate foliation coupled with diffusive
446 pressure solution creep can reduce fault zone strength by 50-70% below Byerlee values
447 ($\mu \approx 0.85$) [*Bos and Spiers*, 2002; *Niemeijer and Spiers*, 2005]. However, this
448 mechanism will only operate in foliated gouges and/or cataclasites at low sliding
449 velocity when the phyllosilicate foliation is interconnected and the rate of mass removal
450 by pressure solution is fast enough to accommodate shear. Phyllosilicate foliations are
451 disrupted at experimental sliding velocities >0.3-1 μm/s (equivalent strain rates >0.3-1
452 s^{-1}) [*Bos and Spiers*, 2001; *Niemeijer and Spiers*, 2005].

453 The frequent juxtaposition of Unit 3 nonfoliated cataclasites and Unit 4 foliated
454 cataclasites within DFDP-1 drillcore may reflect deformation accommodated at various
455 sliding velocities within these materials (Figures 3 and 4a). However, the occurrence of
456 recycled fault gouge clasts, relict pseudotachylyte, and enhanced alteration in the
457 smectite-bearing Unit 5 PSZ gouges suggest that repeated slip events occurred
458 preferentially in these materials (e.g., Figures 4g and 6a). Therefore, understanding the
459 frictional properties of these materials remains a primary research objective [*Boulton*
460 *et al.*, 2012, 2014; *Niemeijer et al.*, 2016]. Although there is currently no evidence that
461 aseismic creep occurs on the Alpine Fault, observations are limited to the past 50 years,
462 a time span covering the late interseismic phase of the seismic cycle [*Evison*, 1971;
463 *Sutherland et al.*, 2007; *Beavan et al.*, 1999, 2009; *Lamb and Smith*, 2013]. It is possible
464 that temporal variations in pore fluid pressure, effective normal stress, shear stress,

sliding velocity, and pore fluid chemistry promote the operation of mechanically diverse deformation mechanisms [e.g., *Smith et al.*, 2011; *Rowe et al.*, 2011].

5.4 Effect of alteration reactions on fault zone permeability

Fault-normal permeability of hanging wall materials decreases with proximity to the highly impermeable Unit 5 PSZ gouges (from c. 10^{-15} m^2 to 10^{-20} m^2) [*Carpenter et al.*, 2014]. These permeability data correspond with the decrease in grain size, an increase in abundance of fault parallel (or subparallel) fine-grained foliations, and/or an increase in pore-infilling, fracture-sealing clay minerals and carbonate with proximity to the PSZ gouges (Figures 4-6) [*Sutherland et al.*, 2012; *Townend et al.*, 2013; *Carpenter et al.*, 2014]. Within alteration zone-fault core lithologic units (Units 2-6), solution-assisted compaction might also lead to significant porosity reduction, further decreasing permeability and promoting pore fluid pressurization, which is another viable weakening mechanism [e.g., *Sibson*, 1991; *Sleep and Blanpied*, 1992; *Wibberley and Shimamoto*, 2003] (e.g., Figures 4c-d). A time-dependent increase in pore fluid pressure within frictionally strong fault material is compatible with repeating seismic failure without the operation of intervening aseismic creep, a deformation pattern consistent with current paleoseismological records of Alpine Fault seismicity [e.g., *Sutherland et al.*, 2007; *Berryman et al.*, 2012; *Howarth et al.*, 2012].

5.5 Implications for the Alpine Fault seismic cycle

Temporal variations in pore fluid pressure can be visualized in the context of an earthquake cycle-model (Figure 11). The creation of fractures within hanging wall and footwall fault-related rocks during an earthquake increases permeability and promotes fluid migration within the alteration zone [e.g., *Caine et al.*, 1998; *Chester and Chester*, 1998; *Mizoguchi and Ueta*, 2013]. While permeability is likely to increase within

alteration and damage zone lithologic units during a seismic event, high velocity sliding can either decrease PSZ gouge permeability through shear-induced compaction [*Tanikawa et al.*, 2012] or increase PSZ gouge permeability through shear- or thermal pressurization-induced dilation [e.g., *Segall and Rice*, 1995; *Samuelson et al.*, 2009; *Garagash*, 2012; *Platt et al.*, 2015]. Within the alteration zone, migration of carbonate-saturated meteoric fluids in chemical disequilibrium with the rock would promote the precipitation of carbonate, and phyllosilicate minerals, resulting in a time-dependent decrease in permeability and sealing. Coseismic increases in permeability may also facilitate up-dip migration of hotter fault zone fluids into the alteration zone [*Sibson*, 1992; *Menzies et al.*, 2016]. The net effect of enhanced fluid migration within the alteration zone is the gradual reduction in porosity and permeability within these materials through a combination of grain-scale healing and fracture sealing through precipitation (which requires advective fluid flow and infiltration) [e.g., *Warr and Cox*, 2001; *Townend et al.*, 2013]. Thus, fault strength increases, and permeability decreases, during the interseismic phase of the earthquake cycle (Figure 11).

A limitation of this qualitative model, derived from data on surface-outcrop fault rocks and supported by results from the shallow DFDP-1 boreholes, is that it does not address lithological, spatial, and temporal variations in fault zone healing rates. Within framework silicate-rich fault core gouges, compaction and frictional strengthening via solution-assisted mass transfer processes occur most rapidly at temperatures ≥150ºC on short time scales (days to weeks or months) [*Renard et al.*, 2000; *Niemeijer et al.*, 2002; *Tenthorey and Cox*, 2006; *Gratier et al.*, 2009, 2011]. However, the healing mechanism in phyllosilicate-rich gouges, such as those described here in DFDP-1A and 1B, is poorly understood. In the San Andreas Fault Observatory at Depth (SAFOD), for example, trioctahedral smectite (saponite)-rich gouges are

514 actively creeping [e.g., *Holdsworth et al.*, 2011]. Laboratory experiments on fault
515 gouge analogues indicate that phyllosilicate-rich gouges do not heal via solid-state or
516 solution-assisted mass transfer [e.g., *Dieterich*, 1978; *Bos and Spiers*, 2000; *Niemeijer*
517 *and Spiers*, 2006]. Products of alteration reactions observed in the smectite-bearing
518 Unit 5 gouges present in DFDP-1A and 1B, as well as other localities along strike of
519 the fault, include calcite and iron hydroxide (Tables 3 and 4) (Figure 4g). Porosity
520 reduction via precipitation of these minerals as cement may be influential in sealing the
521 fault core gouges in the upper ~2 km of the fault (Figure 11).

522 Permeability changes in strike-slip fault zones as a function of gouge
523 compaction, crack sealing, and fluid flow from depth have been modeled quantitatively
524 [*Gratier et al.*, 2003, *Gratier and Gueydan*, 2007]. According to these models, late
525 interseismic lithostatic pore fluid overpressures develop most quickly at two different
526 depth intervals: in the upper crust (30ºC<T<90ºC) where calcite is available for mass
527 transfer and relatively fast sealing of veins, and at depth (150ºC<T<300ºC) due to
528 increased quartz solubility combined with inflow of fluids from the lower crust. In turn,
529 depth-dependent lithostatic pore fluid pressures develop within 270 years following an
530 earthquake [*Gratier and Gueydan*, 2007]. Although these models depend critically on
531 the kinetics of the involved dissolution and precipitation reactions as well as on
532 diffusion rates, 270 years is within the recurrence interval of Alpine Fault earthquakes
533 (329±68 years) [*Berryman et al.*, 2012].

534 Abundant evidence exists for persistent 100 m to 1 km-thick damage zones in
535 the shallow crust (< 3 km) [e.g., *Chester and Logan*, 1986; *Li et al.*, 1990, 2000, 2004;
536 *Mitchell and Faulkner*, 2009; *Yang et al.*, 2011]. However, within the fault core-
537 alteration zone at Gaunt Creek, and elsewhere along the Alpine Fault, hanging wall
538 fractures have been sealed by authigenic precipitation of calcite and phyllosilicates

[*Sutherland et al.*, 2012; *Townend et al.*, 2013] (Table 3) (Figures 5c, 5f, and 7-9). This sealing has decreased fault normal permeability and increased rock mass competency, potentially promoting interseismic strain buildup (Figure 11). Further research aimed towards understanding mass transfer processes within the fault zone is integral to underpinning the mechanisms responsible for variations in late interseismic fault zone strength [e.g., *Finzi et al.*, 2011].

To quantify the physical processes driving the seismic cycle on the Alpine Fault, better constraints on mineral reactions, reaction rates, diffusion rates, compaction, and healing rates in the lab and in naturally deformed fault rocks are needed [e.g., *Renard et al.*, 2000, 2012; *Gratier et al.*, 2003]. In addition, geophysical and geochemical observations of fluid flux during interseismic, coseismic, and postseismic periods, are needed for numerical models that quantify how fluid migration, porosity, permeability, and rock strength evolve at depth and during exhumation [*Menzies et al.*, 2016]. Incorporating permeability and fluid pressure evolution variables into empirical rate- and state-dependent constitutive laws will ultimately better constrain how fluid-rock interactions influence fault strength evolution, strain accumulation, and the timing and mode of earthquake rupture nucleation [e.g., *Sibson*, 1992; *Segall and Rice*, 1995; *Sibson and Rowland*, 2003; *Hillers and Miller*, 2006, *Ben-Zion*, 2008; *Samuelson et al.*, 2009].

6 Conclusions

1. On the Alpine Fault at Gaunt Creek, a fault core extends into the hanging wall up to c. 20-30 m from the PSZ assuming that the first documented occurrence of retrogressed mineral assemblages in the Unit 2 brown–green–black

562 ultramylonites represents the maximum extent of alteration zone processes
563 within the fault core.
564 2. The presence of the low-temperature clay minerals montmorillonite and
565 kaolinite, along with the high measured LOI values, in the brown smectite-
566 bearing Unit 5 PSZ gouges suggests that these units are the most highly altered
567 rocks recovered. The presence of variably comminuted vein calcite and
568 secondary calcite cement is reflected in the major element geochemistry of the
569 PSZ gouges, where CaO concentrations are higher than in adjacent Unit 6 lower
570 cataclasites.
571 3. Similar montmorillonite-bearing Unit 5 PSZ gouges were collected from thrust
572 segments of the central Alpine Fault at Little Man River, Waikukupa River, and
573 Robinson Creek, an along-strike distance of 120 km. These field observations
574 delimit the minimum near-surface extent of principal slip zone materials
575 recovered during DFDP-1.
576 4. Minerals, microstructures, and major elements measured in the DFDP-1 fault
577 rocks reflect seismic cycle processes. Within the alteration zone, off-fault
578 damage has created brittle fractures that facilitate the infiltration of meteoric
579 and (potentially) metamorphic or rock-exchanged hydrothermal fluids. These
580 fluids promote carbonate and phyllosilicates precipitation, which in turn
581 gradually decrease porosity and permeability through a combination of grain-
582 scale healing and fracture sealing (e.g., Table 7, Figures 3-6 and 11).
583 5. Interseismic increases in fault strength promoted by fluid-rock interactions
584 allow the Alpine Fault to accumulate the stored elastic strain energy necessary
585 for earthquake rupture nucleation and propagation [e.g., *Kanamori and*
586 *Brodsky*, 2001].

587 **Acknowledgements**

588 The following people, companies, and institutions made the Deep Fault Drilling Project
589 (DFDP-1) successful: Horizon Drilling, Alex Pyne, the New Zealand Department of
590 Conservation, the Marsden Fund, GNS Science, Victoria University of Wellington and
591 the Universities of Otago, Auckland, Canterbury, Liverpool, and Bremen. The first
592 author would like to thank Mark Raven, Brent Pooley, Damian Walls, and Carmel
593 Pinnington for excellent technical assistance. The manuscript benefited greatly from
594 reviews by Jim Evans and an anonymous reviewer. All data are located in
595 supplementary material. CB and CDM are supported by NERC grant NE/J02449/1.

596 **References**

597 Ague, J.J. (1994). Mass transfer during Barrovian metamorphism of pelites, south-
598 central Conneticut. I: Evidence for changes in composition and volume, *Am. J. Sci.*,
599 *294*, 989-1057.

600 Barth, N., V. Toy, R. Langridge, and R. Norris (2012), Scale dependence of oblique
601 plate-boundary partitioning: New insights from LiDAR, central Alpine
602 fault, New Zealand, *Lithosphere*, doi:10.1130/L201.1.

603 Barth N.C., C. Boulton, B.M. Carpenter, G.E. Batt, and V.G. Toy (2013), Slip
604 localization on the southern Alpine Fault, New Zealand, *Tectonics*, *32*, 1-21.

605 Batt G., S. Baldwin, M. Cottam, P. Fitzgerald, M. Brandon, and T. Spell (2004),
606 Cenozoic plate boundary evolution in the South Island of New Zealand:
607 New thermochronological constraints, *Tectonics*, *23*, TC4001, doi:10.1029/
608 2003TC001527.

609 Beavan J., M. Moore, C. Pearson, M. Henderson, B. Parsons, S. Bourne, P. England,

610 D. Walcott, G. Blick, D. Darby, and K. Hodgkinson (1999), Crustal deformation
611 during 1994-1998, due to oblique continental collision in the central
612 Southern Alps, New Zealand, and implications for seismic potential of
613 the Alpine fault, *J. Geophys. Res.*, *104*(B11), 25233–25255,
614 doi:10.1029/1999JB900198.

615 Beavan, J., Denys, P., Denham, M., Hager, B., Herring, T. and P. Molnar (2010),
616 Distribution of present-day vertical deformation across the Southern Alps, New
617 Zealand, from 10 years of GPS data, *Geophs. Res. Lett.*, *37*, L16305,
618 doi:10.1029/2010GL044165.

619 Berryman, K., S. Beanland, A. Cooper, H. Cutten, R. Norris, and P. Wood (1992),
620 The Alpine Fault, New Zealand: variation in Quaternary structural style
621 and geomorphic expression. *Annales Tectonicae IV*, 126–163.

622 Ben-Zion, Y. (2008), Collective behavior of earthquakes and faults: Continuum-
623 discrete transitions, progressive evolutionary changes, and different dynamic
624 regimes, *Rev. Geophy.*, *46*, RG4006, doi:10.1029/2008RG000260.

625 Berryman, K.B., U.A. Cochran, K.J. Clark, G.P. Biasi, R.M. Langridge, and P.
626 Villamor (2012), Major earthquakes occur regularly on an isolated plate boundary
627 fault, *Science*, *29*(336), 1690-1693, doi:10.1126/science.1218959.

628 Bos, B., and C. Spiers (2001), Experimental investigation into the microstructural
629 and mechanical evolution of phyllosilicate-bearing fault rock under conditions
630 favouring pressure solution, *J. Struct. Geol.*, *23*, 1187–1202.

631 Bos, B., and Spiers, C. (2002), Frictional-viscous flow of phyllosilicate-bearing fault
632 rock: Microphysical model and implications for crustal strength profiles,

633 *J. Geophys. Res.*, *107*(B2). doi:10.1029/2001JB000301.

634 Boulton, C., B.M. Carpenter, V. Toy, and C. Marone (2012), Physical properties of
635 surface outcrop cataclastic fault rocks, Alpine Fault, New Zealand, *Geochem.*
636 *Geophys. Geosys.*, *13*, Q01018, doi:10.1029/2011GC003872.

637 Boulton, C., D. Moore, D. Lockner, V. Toy, J. Townend, and R. Sutherland (2014),
638 Frictional strength and stability of exhumed fault gouges in DFDP-1 cores,
639 Alpine Fault, New Zealand, *Geophys. Res. Lett.*, *41*, doi:10.1002/2013GL058236.

640 Caine, J., J. Evans, and C. Forster (1996), Fault zone architecture and permeability
641 structure. *Geology*, *24*(11), 1025–1028.

642 Cande, S.C., and J.M. Stock (2004), Pacific-Antarctic-Australia motion and the
643 formation of the Macquarie Plate, *Geophys. J. Int.*, *157*, 399-414.

644 Carpenter, B.M., H. Kitajima, and D.M. Saffer (2014), Permeability and elastic
645 properties of the active Alpine Fault, New Zealand: measurements on DFDP-1 drill
646 core, *Earth Planet. Sci. Lett.*, *390*, 45-51, doi:10.1016/j.epsl.2013.12.023.

647 Carter, R.M., and R.J. Norris (1976), Cainozoic history of southern New Zealand: An
648 accord between geological observations and plate tectonic predictions, *Earth Planet.*
649 *Sci. Lett.*, *31*, 85-94.

650 Chamberlain, C., M. Poage, D. Craw, and R. Reynolds (1999) Topographic
651 development of the Southern Alps recorded by the isotopic composition of authigenic
652 clay minerals, South Island, New Zealand, *Chem. Geol*., *155*, 279–294.

653 Chen, J., X. Yang, S. Ma, and C.J. Spiers (2013), Mass removal and clay mineral
654 dehydration/rehydration in carbonate-rich surface exposures of the 2008 Wenchuan

655 Earthquake fault: geochemical evidence and implications for fault zone evolution and
656 coseismic slip, *J. Geophys. Res., 118*, 474-496, doi:10.1002/jgrb50089.

657 Chester, F.M., and J.M. Logan (1986), Implications for mechanical properties of
658 brittle faults from observations of the Punchbowl fault zone, California, *Pure Appl.*
659 *Geophys., 124*, 79-106.

660 Chester, F., and N. Higgs (1992), Multimechanism friction constitutive model for
661 ultrafine quartz gouge at hypocentral conditions, *J. Geophys. Res., 97*(B2), 1859–
662 1870.

663 Chester, F., and J. Chester (1998), Ultracataclasite structure and friction processes of
664 the Punchbowl fault, San Andreas system, California, *Tectonophysics*, *295*, 199-221.

665 Chester, F.M., J.P. Evans, and R.L. Biegel (1993), Internal structure and weakening
666 mechanisms of the San Andreas fault, *J. Geophys. Res., 98*, 771-786.

667 Collettini, C., and R.E. Holdsworth (2004), Fault zone weakening and character of
668 slip along low-angle normal faults: insights from the Zuccale fault, Elba, Italy, *J.*
669 *Geol. Soc. London*, *161*, 1039-1051.

670 Collettini, C., Niemeijer, A., Viti, C., and C. Marone (2009), Fault zone fabric and
671 fault weakness, *Nature, 462*, 907- 910, doi:10.1038/nature08585.

672 Cooper, A.F. and R.J. Norris (1994), Anatomy, structural evolution and slip rate of a
673 plate-boundary thrust: The Alpine fault at Gaunt Creek, Westland, New Zealand, *Geol.*
674 *Soc. Am. Bull., 106*, 627-633.

675 Cooper, A., and R.J. Norris (2011), Inverted metamorphic sequences in Alpine fault
676 mylonites produced by oblique shear within a plate boundary fault zone, New

677 Zealand, *Geology*, *39*(11), 1023–1026. doi:10.1130/G32273.

678 Craw, D. (1988), Shallow level penetration of metamorphic fluids in a high uplift rate
679 mountain belt, Southern Alps, New Zealand, *J. Met. Geol.*, 6, 1-16.

680 Craw, D., and J.R. Campbell (2004), Tectonic and structural setting for active
681 mesothermal gold vein systems, Southern Alps, New Zealand, *J. Struct. Geol.*, *26*,
682 995-1005.

683 Cox, S.C. (1993), *Veins, Fluid, Fractals, Scale and Schist: an investigation of fluid*
684 *rock interaction during deformation of the Torlesse Terrane, New Zealand*, PhD
685 thesis. Dunedin, University of Otago.

686 Deer, W.A., R.A. Howie, and J. Zussman (1992), *An Introduction to Rock-Forming*
687 *Minerals*, 2nd edition. Essex, Longman Group UK Limited.

688 Easterbrook, L. (2010), *The Alpine Fault Zone Along the Waitangi-taona River, West*
689 *Coast, New Zealand*, MSc thesis. Dunedin, University of Otago.

690 Evans, J.P., and F.M. Chester (1995), Fluid-rock interaction in faults of the San Andreas
691 system: Inferences from San Gabriel fault rock geochemistry and microstructures, *J.*
692 *Geophys. Res., 100*, 13007-13020.

693 Evison, F. (1971), Seismicity of the Alpine Fault, New Zealand. Recent Crustal
694 Movements, *Roy. Soc. N. Zeal. Bull.*, *9*, 161–165.

695 Finzi, Y., E.H. Hearn, V. Lyakhovsky, and L. Gross (2011), Fault-zone healing
696 effectiveness and the structural evolution of strike-slip fault systems, *Geophys. Jour.*
697 *Inter.*, *186*, 963-970.

698 Gaina, C., D.R. Mueller, J.-Y. Royer, J. Stock, J. Hardebeck, and P. Symonds (1998),
699 The tectonic history of the Tasman Sea: a puzzle with 13 pieces, *J. Geophys. Res.*,
700 *103*(6), 12413-12433, doi:10.1029/98JB00386.

701 Garagash, D. (2012), Seismic and aseismic slip pulses driven by thermal
702 pressurization of pore fluid, *J. Geophys. Res.*, *117*, B04314,
703 doi:10.1029/2011JB008889.

704 Goddard, J.V., and J.P. Evans (1995), Chemical changes and fluid-rock interaction in
705 fault of crystalline thrust sheets, northwestern Wyoming, U.S.A, *J. Struct. Geol.*, 17,
706 533-547.

707 Grant, J.A. (1986), The isocon diagram; a simple solution to Gresens' equation for
708 metasomatic alteration, *Econ. Geol.*, *81*, 1976-1982.

709 Gratier, J., P. Favreau, and F. Renard (2003), Modeling fluid transfer along California
710 faults when integrating pressure solution crack sealing and compaction
711 processes, *J. Geophys. Res.*, *108*(B2), doi:10.1029/2001JB000380.

712 Gresens, R.L. (1967), Composition-volume relationships of metasomatism. *Chem.*
713 *Geol.*, *2*, 47-65.

714 Hickman, S., R. Sibson, and R. Bruhn (1995), Introduction to special section:
715 Mechanical involvement of fluids in faulting. *J. Geophys. Res.*, *100*(B7), 12831-
716 12840.

717 Hillers, G., and S. Miller (2007), Dilatancy controlled spatiotemporal slip evolution
718 of a sealed fault with spatial variations of the pore pressure, *Geophys. J. Inter.*, *168*,
719 431–445, doi:10.1111/j.1365-246X.2006.03167.

720 Holland, T.J.B., and R. Powell (1998), An internally consistent thermodynamic data
721 set for phases of petrological interest, *J. Met. Geol.*, *16*, 309-343.

722 Imber, J., R.E. Holdsworth, S.A.F. Smith, S.P. Jefferies, and C. Collettini (2008),
723 Frictional-viscous flow, seismicity and the geology of weak faults: a review and future
724 directions, in *The Internal Structure of Fault Zones: Implications for Mechanical and*
725 *Fluid-Flow Properties*, *Geol. Soc. London Spec. Pub.*, vol. 299, edited by Wibberley,
726 C.A.J., W. Kurz, J. Imber, R.E. Holdsworth, and C. Collettini pp. 151-172, Geol. Soc.
727 London, London.

728 Isaacs, A.J., J.P. Evans, P.T. Kolesar, and T. Nohara (2008), Composition,
729 microstructures, and petrophysics of the Mozumi fault, Japan: In situ analyses of fault
730 zone properties and structure in sedimentary rocks from shallow crustal levels, *J.*
731 *Geophys. Res.*, *113*, B12408, doi:10.1029/2007JB005314.

732 Janecke, S.U., and J.P. Evans (1988), Feldspar-influenced rock rheologies, *Geology*
733 *16*(12), 1064-1067.

734 King, G.C.P. (1986), Speculations on the Geometry of the Initiation and Termination
735 Processes of Earthquake Rupture and its Relation to Morphology and Geological
736 Structure. *Pure Appl. Geophys.*, *124*, 567-585.

737 Lamb, S., and E. Smith (2013), The nature of the plate interface and driving force of
738 interseismic deformation in the New Zealand plate-boundary zone, revealed by the
739 continuous GPS velocity field, *J. Geophys. Res.*, *118*, doi:10.1002/jgrb.50221.

740 Lamb, S., E. Smith, T. Stern, and E. Warren-Smith (2015), Continent-scale strike-slip
741 on a low-angle fault beneath New Zealand's Southern Alps: Implications for crustal
742 thickening in oblique collision zones, *Geochem., Geophys., Geosys.*, *16*,
743 doi:10.1002/2015GC005990.

744 Lamb, S., N. Mortimer, E. Smith, and G. Turner (2016), Focusing of relative plate
745 motion at a continental transform fault: Cenozoic dextral displacement >700 km on
746 New Zealand's Alpine Fault, reversing >225 km of Late Cretaceous sinistral motion.
747 *Geochem., Geophys., Geosys*., doi:10.1002/2015GC006225.

748 Landis, C.A., and D.S. Coombs (1966), Metamorphic belts and orogenesis in southern
749 New Zealand, *Tectonophysics*, 4, 501-518.

750 Li, Y.G., P.G. Leary, K. Aki, and P. Malin (1990), Seismic trapped modes in the
751 Oroville and San Andreas fault zones, *Science*, *249*, 763-766.

752 Li, Y.G., J.E. Vidale, K. Aki, and F. Xu, (2000), Depth-dependent structure of the
753 Landers fault zone using fault zone trapped waves generated by aftershocks, *J.*
754 *Geophys. Res., 105*, 6237-6254.

755 Li, Y.G., J.R. Vidale, and E. Cochran (2004), Low-velocity damaged structure of the
756 San Andreas Fault at Parkfield from fault zone trapped waves, *Geophys. Res. Lett., 31*,
757 L12S06, doi:10.1029/2003GL019044.

758 Little, T.A., Cox, S., Vry, J.K., and G. Batt (2005), Variations in exhumation level and
759 uplift-rate along the oblique-slip Alpine fault, central Southern Alps, New Zealand,
760 *Geol. Soc. Am. Bull., 117(5-6)*, 707-723.

761 Ma, S., and G.C. Beroza (2008), Rupture dynamics on a biomaterial interface for
762 dipping for dipping faults *Bull. Seismol. Soc. Am.*, *98*(4), 1642-1658.

763 McClintock, M.K. (1999), *Alpine Fault Zone structure and tectonometamorphic*
764 *evolution, Makawhio River, South Westland*, BSc (Hons) thesis. Dunedin, University
765 of Otago.

766 McClintock, M.K., and A.F. Cooper (2003), Geochemistry, mineralogy, and
767 metamorphic history of kyanite-orthoamphibole-bearing Alpine Fault mylonite, South
768 Westland, New Zealand, *N. Z. J. Geol. Geophys.*, *46*, 47-62,
769 doi:10.1080/00288306.2003.9514995.

770 Menzies, C.D., D.A.H. Teagle, D. Craw, S.C. Cox, A.J. Boyce, and D. Barrie (2014),
771 Incursion of meteoric waters into the ductile regime in an active orogeny, *Earth*
772 *Planet. Sci. Lett.*, *399*, 1-14.

773 Menzies, C.D., D.A.H. Teagle, S. Niedermann, S.C. Cox, D. Craw, M. Zimmer, M.J.
774 Cooper, J. Erzinger (2016), The fluid budget of a continental plate boundary fault:
775 Quantification from the Alpine Fault, New Zealand, *Earth Planet. Sci. Lett.*, *445*, 125-
776 135, doi:10.1016/j/epsl.2016.03.046.

777 Mitchell, T.M., and D.R. Faulkner (2009), The nature and origin of off-fault damage
778 surrounding strike-slip fault zones with a wide range of displacements: A field study
779 from the Atacama fault system, northern Chile, *J. Struct. Geol.*, *31*, 802-816.

780 Mizoguchi, K., and K. Ueta (2013), Microfractures within the fault damage zone
781 record the history of fault activity, *Geophys. Res. Lett.*, *40*, 1-5, doi:10.1002/grl50469.

782 Molnar, P., T. Atwater, J. Mammerickx, and S.M. Smith (1975), Magnetic anomalies,
783 bathymetry and the tectonic evolution of the South Pacific since the Late Cretaceous,
784 *Geophys. J. Int.*, *40*(3), 383-420.

785 Moore, D.E., and D.A. Lockner (2004), Crystallographic controls on the frictional
786 behavior of dry and water-saturated sheet structure minerals, *J. Geophys. Res.*,
787 *109*(B03401). doi:10.1029/2003JB002582.

788 Mortimer, N. (2004), New Zealand's geological foundations. *Gondwana Res.*,

7, 261–272.

Meunier, A. (2005), *Clays*, Springer-Verlag Berlin, 472 pp.

Nathan, S. (1976), Geochemistry of the Greenland Group (Early Ordovician), New Zealand, *N. Z. J. Geol. Geophys*, *19*, 683-706.

Nathan, S., (1998), Petrographic notes on samples from the Glasgow and Victoria Ranges. Immediate Report.

Niemeijer, A., and C.J. Spiers (2005), Influence of phyllosilicates on fault strength in the brittle-ductile transition: insights from rock analogue experiments, *Geological Society London Special Publications*, *245*, 303–327.

Niemeijer, A.R., C. Boulton, V.G. Toy, J. Townend, and R. Sutherland (2016), Large-displacement, hydrothermal frictional properties of DFDP-1 fault rocks, Alpine Fault, New Zealand: Implications for deep rupture propagation, *J. Geophys. Res.*, 121, doi:10.1002/2015JB012593.

Norris, R.J., and A.F. Cooper, (1995), Origin of small-scale segmentation and transpressional thrusting along the Alpine fault, New Zealand, *Geol. Soc. Am. Bull.*, *107*, 231-240.

Norris, R.J., and A.F. Cooper (2007), The Alpine Fault, New Zealand: Surface geology and field relationships, in *A Continental Plate Boundary: Tectonics at South Island, New Zealand*, *Geophys. Monogr. Ser.*, vol. 175, edited by D. Okaya, T. Stern, and F. Davey, pp. 159-178, AGU, Washington, D.C., doi:10.1029/175GM09.

O'Hara, K. (1988), Fluid flow and volume loss during mylonitization- An origin for phyllonite in an overthrust setting, North Carolina, USA, *Tectonophys.*, *156*, 21-36.

811 Pitcairn, I.K. (2004), *Sources of fluids and metals in orogenic gold deposits: The Otago*
812 *schist's, New Zealand,* PhD thesis. Southampton, University of Southampton.

813 Pitcairn, I.K., D.A.H. Teagle, D. Craw, G.R. Olivo, R. Kerrich, and T.S. Brewer (2006),
814 Sources of metals and fluids in orogenic gold deposits: Insights from the Otago and
815 Alpine Schists, New Zealand, *Econ. Geol.*, *101*, 1525-1546.

816 Platt, J.D., R.C. Viesca, and D.I. Garagash (2015), Steadily propagating slip pulses
817 driven by thermal decomposition, *J. Geophys. Res. Solid Earth*, *120*,
818 doi:10.1002/2015JB012200.

819 Prior, D.J. (1988), *Deformation processes in the Alpine Fault Mylonites, South Island,*
820 *New Zealand,* PhD thesis. Leeds, University of Leeds.

821 Pytte, A.M., and R.C Reynolds (1988), The thermal transformation of smectite to illite,
822 in *Thermal Histories of Sedimentary Basins*, edited by T.H. McCulloh and N.D. Naeser,
823 pp. 133-140, Springer, New York.

824 Rattenbury, M.S. (1987), *Fraser Complex and Alpine Fault tectonics, central Westland,*
825 *New Zealand,* PhD thesis. Dunedin, University of Otago.

826 Reed, J.J. (1958), Granites and mineralization in New Zealand, *N. Z. J. Geol. Geophys*,
827 *1*, 47-64, doi:10.1080/00288306.1958.10422794.

828 Reed, J.J. (1964), Mylonites, cataclasites, and associated rocks along the Alpine Fault,
829 South Island, New Zealand, *N. Z. J. Geol. Geophys*, *7*, 645-684.

830 Renard, F., J. Gratier, and B. Jamtveit (2000), Kinetics of crack-sealing, intergranular
831 pressure solution, and compaction around active faults, *J. Struct. Geol.*,, *22*, 1395–
832 1407.

833 Renard, F., S. Beaupretre, C. Voisin, D. Zigone, T. Candela, D.K. Dysthe, and J-P.
834 Gratier (2012), Strength evolution of a reactive frictional interface is controlled by the
835 dynamics of contacts and chemical effects, *Earth Planet. Sci. Lett.*, *341-344*, 20-34.

836 Roser, B.P., and R.J. Korsch (1999), Geochemical characterization, evolution and
837 source of a Mesozoic accretionary wedge: the Torlesse terrane, New Zealand, *Geol.*
838 *Mag.*, *136*, 493-512.

839 Roser, B.P., R.H. Grapes, and K. Palmer (1995), XRF analyses of sandstones and
840 argillites from the Torlesse terrane, New Zealand. Research School of Earth Science,
841 Victoria University, Wellington Geology Board Studies Publication 15, 40 p.

842 Rowe, C.D., F. Meneghini, and J. Casey Moore (2011), Textural record of the seismic
843 cycle: strain-rate variation in an ancient subduction thrust, in *Geology of the Earthquake*
844 *Source: A Volume in Honour of Rick Sibson*, *Geol. Soc. London Spec. Pub.*, vol. 359,
845 edited by Fagereng A., V.G. Toy, and J.V. Rowland, pp. 77-95, Geol. Soc. London,
846 London.

847 Samuelson, J., Elsworth, D., and C. Marone (2009), Shear-induced dilatancy of fluid-
848 saturated faults: Experiment and theory, *J. Geophys. Res.,114*, B12404,
849 doi:10.1029/2008JB006273.

850 Segall, P., and J.R. Rice (1995), Dilatancy, compaction, and slip instability of a
851 fluid-infiltrated fault, *J. Geophys. Res*., *100*, 22155–22171, doi:10.1029/95JB02403

852 Schleicher, A.M., S.N. Tourscher, B.A. van der Pluijm, and L.N. Warr (2009),
853 Constraints on mineralization, fluid-rock interaction, and mass transfer during faulting
854 at 2-3 km depth from the SAFOD drill hole, *J. Geophys. Res.*, *114*, B04202,
855 doi:10.1029/2008JB006092.

856 Schleicher, A.M., R. Sutherland, J. Townend, V.G. Toy, and B.A. van der Pluijm
857 (2015), Clay mineral formation and fabric development in the DFDP-1B borehole,
858 central Alpine Fault, New Zealand, *N. Z. J. Geol. Geophys.*, *58*(1), 13-21,
859 doi:10.1080/00288306.2014.979841.

860 Scholz, C.H. (2002). *The Mechanics of Earthquakes and Faulting*, 2nd ed. Cambridge
861 University Press, New York.

862 Schulz, S.E., and J.P. Evans (1998), Spatial variability in microscopic deformation
863 and composition of the Punchbowl fault, Southern California: implications for
864 mechanisms, fluid-rock interaction, and fault morphology, *Tectonophys.*, *295*, 223-
865 244, doi:10.1016/S0040-1951(98)00122-X.

866 Schulz, S.E., and J.P. Evans (2000), Mesoscopic structure of the Punchbowl fault,
867 southern California, and the geologic and geophysical structure of active strike-slip
868 faults, *J. Struct. Geol.*, *22*, 913-930, doi:10.1016/S0191-8141(00)00019-5.

869 Scott, H.R. (2012). *Cataclastic processes within the Alpine fault zone*. MSc thesis.
870 Dunedin, University of Otago.

871 Sibson, R.H. (1977), Fault rocks and fault mechanisms, *Geol. Soc. London J.*, *133*, 191-
872 213.

873 Sibson, R.H. (1982), Fault Zone Models, Heat Flow, and the Depth Distribution
874 of Earthquakes in the Continental Crust of the United States, *Bull. Seis. Soc. Am.*,
875 *72*(1), 151–163.

876 Sibson, R.H. (1991), Loading of faults to failure. *Bull. Seis. Soc. Am.*, *81*(6), 2493–
877 2497.

878 Sibson, R.H. (1992), Implications of fault-valve behaviour for rupture nucleation and
879 recurrence, *Tectonophysics*, *211*, 283-293.

880 Sibson, R.H. (2003), Thickness of the seismic slip zone. *Bull. Seis. Soc. Am.*, *93*,
881 1169–1178, doi:10.1785/0120020061.

882 Sibson, R.H., and J.V. Rowland (2003), Stress, fluid pressure and structural
883 permeability in seismogenic crust, North Island, New Zealand, *Geophys. J. Int.*, *154*,
884 584-594.

885 Sibson, R.H, S.H. White, and B.K. Atkinson (1979), Fault rock distribution and
886 structure within the Alpine Fault Zone: a preliminary account, in *The Origin of the*
887 *Southern Alps*, *Bull. Roy. Soc. N. Z.*, vol. 18, edited by Walcott R.I., and M.M.
888 Cresswell, pp. 55-65.

889 Simpson, G.D.H. (1992), *Quaternary evolution of the Alpine Fault Zone, and a*
890 *mineralogical/microstructural study of the schist-mylonite transition*, BSc (Hons)
891 thesis. Dunedin, University of Otago.

892 Simpson, G.D.H., A.F. Cooper, and R.J. Norris (1994), Late Quaternary evolution of
893 the Alpine Fault Zone at Paringa, South Westland, New Zealand, *N. Z. J. Geol.*
894 *Geophys*, *37*, 49-58.

895 Sleep, N.H., and M.L. Blanpied (1992), Creep, compaction, and the weak rheology
896 of major faults, *Nature*, *359*, 687–692.

897 Smith, S.A.F., R.E. Holdsworth, C. Collettini, and P Ma (2011), The microstructural
898 character and mechanical significance of fault rocks associated with a continental low-
899 angle normal fault: the Zuccale Fault, Elba Island, Italy, in *Geology of the Earthquake*
900 *Source: A Volume in Honour of Rick Sibson*, *Geol. Soc. London Spec. Pub.*, vol. 359,

edited by Fagereng A., V.G. Toy, and J.V. Rowland, pp. 97-113, Geol. Soc. London, London.

Sutherland, R. (1995), The Australia-Pacific boundary and Cenozoic plate motions in the SW Pacific; some constraints from Geosat data, *Tectonics*, *14*(4), 819-831.

Sutherland, R. (1999), Basement geology and tectonic development of the greater New Zealand region: an interpretation from regional magnetic data, *Tectonophys.*, *308*(3), 341-362, doi:10.1016/S0040-1951(99)00108-0.

Sutherland, R., F. Davey, and J.P. Beavan (2000), Plate boundary deformation in South Island, New Zealand, is related to inherited lithopheric structure, *Earth Planet. Sci. Lett.*, *177*, 141–151.

Sutherland, R., D. Eberhart-Phillips, R.A. Harris, T.A. Stern, and 15 others (2007), Do great earthquakes occur on the Alpine fault in central South Island, New Zealand?, in *A Continental Plate Boundary: Tectonics at South Island, New Zealand*, *Geophys. Monogr. Ser.*, edited by D. Okaya et al., pp. 235-251, AGU, Washington, D.C.

Sutherland, R., V. Toy, J. Townend, J. Eccles, and 18 others (2011), Operations and well completion report for boreholes DFDP-1A and DFDP-1B, Deep Fault Drilling Project, Alpine Fault, Gaunt Creek, New Zealand. GNS Science Report, Volume 2011/48: Lower Hutt, NZ, Institute of Geological & Nuclear Sciences 70 p.

Sutherland, R., V.G. Toy, J. Townend, S.C. Cox, and 15 others (2012), Drilling reveals fluid control on architecture and rupture of the Alpine Fault, New Zealand, *Geology*, *40*, 1143-1146, doi:10.1130/G33614.1.

Tanikawa, W., H. Mukoyoshi, O. Tadai, T. Hirose, A. Tsutsumi, and W. Lin (2012), Velocity dependence of shear-induced permeability associated with frictional

924 behavior in fault zones of the Nankai subduction zone, *J. Geophys. Res*., 117,
925 B05405, doi:10.1029/2011JB008956.

926 Tembe, S., D.A. Lockner, and Tf. Wong (2010), Effect of clay content and
927 mineraology on frictional sliding behavior of simulated gouges: Binary and ternary
928 mixtures of quartz, illite, and montmorillonite, *J. Geophys. Res., 115,* B03416,
929 doi:10.1029/2009JB006383.

930 Totten, M.W., M.A. Hanan, D. Knight, and J. Borges (2002). Characteristics of
931 mixed-layer smectite/illite density separates during burial diagenesis, *Am. Min.*,
932 *87*(11-12), 1571-1579, doi:10.2138/am-2002-11-1207.

933 Townend, J., R. Sutherland, V.G. Toy, J.D. Eccles, C.J. Boulton, S.C. Cox, and D.
934 McNamara (2013), Late-interseismic state of a continental plate-bounding fault:
935 petrophysical results from DFDP-1 wireline and core analysis, Alpine fault, New
936 Zealand, *Geochem., Geophys., Geosyst*., *14*, doi:10.1002/ggge/20236.

937 Toy, V.G. (2007), *Rheology of the Alpine Fault Mylonite Zone: Deformation Processes*
938 *and Below the Base of the Seismogenic Zone in a Major Plate Boundary Structure*, PhD
939 thesis. Dunedin, University of Otago.

940 Toy, V.G., D.J. Prior, and R.J. Norris (2008), Quartz textures in the Alpine fault
941 mylonites: influence of pre-existing preferred orientations on fabric development
942 during progressive uplift, *J. Struct. Geol., 30,* 602-621.

943 Toy, V.G., D. Craw, A.F. Cooper, and R.J. Norris (2010), Thermal regime in the central
944 Alpine Fault zone, New Zealand: Constraints from microstructures, biotite chemistry,
945 and fluid inclusion data, *Tectonophys.*, doi:10.1016/j.tecto.2009.12.013.

946 Toy, V.G., S. Ritchie, and R.H. Sibson (2011), Diverse habitats of pseudotachylytes in
947 the Alpine Fault Zone and relationships to current seismicity, in *Geology of the*
948 *Earthquake Source: A Volume in Honour of Rick Sibson*, *Geol. Soc. London Spec. Pub.*,
949 vol. 359, edited by Fagereng A., V.G. Toy, and J.V. Rowland, pp. 115-133, Geol. Soc.
950 London, London.

951 Toy, V.G., C.J. Boulton, R. Sutherland, J. Townend, R.J. Norris, T.A. Little, D.J. Prior,
952 E. Mariani, D. Faulkner, C.D. Menzies, H. Scott, and B.M. Carpenter (2015), Fault rock
953 lithologies and architecture of the central Alpine fault, New Zealand, revealed by
954 DFDP-1 drilling, *Lithosphere*, doi:10.1130/L395.1

955 Tulloch, A.J., and K. Palmer (1990), Tectonic implications of granite cobbles from the
956 mid-Cretaceous Pororari Group, southwest Nelson, New Zealand, *N. Z. J. Geol.*
957 *Geophys*, *33*(2), 205-217.

958 Tulloch, A.J., J. Ramezani, D.L. Kimbrough, K. Faure, and A.H. Allibone (2009),
959 U-Pb geochronology of mid-Paleozoic plutonism in western New Zealand:
960 implications for S-type granite generation and growth of the east Gondwana
961 margin, *Geol. Soc. Am. Bull.*, *121*, 1236–1261.

962 Vry J.K., A.C. Storkey, and C. Harris (2001), Role of fluids in the metamorphism
963 of the Alpine Fault Zone, *J. Met. Geol.*, *19*, 21–31.

964 Vry, J., R. Powell, K.M. Golden, and K. Peterson (2009), The role of exhumation in
965 metamorphic dehydration and fluid production, *Nat. Geosci.*, *3*, 31-35.

966 Walcott, R.I. (1984), Reconstructions of the New Zealand region for the Neogene,
967 *Palaeo., Palaeo., Palaeo*., *46*, 217-231.

968 Warr, L.N. and S. Cox (2001), Clay mineral transformations and weakening
969 mechanisms along the Alpine Fault, New Zealand, in *The nature and tectonic*
970 *significance of fault zone weakening: Geol. Soc. London Spec. Pub.,* vol. 186, edited
971 by R.E. Holdsworth, R.A. Strachan, J.F. Magloughlin, and R.J. Knipe, pp. 85-101,
972 Geol. Soc. London, London.

973 Wellman, H.W. (1953), Data for the study of Recent and late Pleistocene faulting in
974 the South Island of New Zealand, *N. Z. J. Sci. Tech., 34B,* 270-288.

975 Wesnousky, S.G. (1988), Seismological and structural evolution of strike-slip faults,
976 *Nature*, *335*, 340-343.

977 Wibberley, C.A.J., and T. Shimamoto (2003), Internal structure and permeability of
978 major strike-slip fault zones: The Median Tectonic Line in Mid Prefecture,
979 southwest Japan, *J. Struct. Geol.*, *25*, 59–78.

980 Wintsch, R.P., and M-W. Yeh (2013), Oscillating brittle and viscous behavior through
981 the earthquake cycle in the Red River Shear Zone: Monitoring flips between reaction
982 and textural softening and hardening, *Tectonophys.*, *587*, 46-62.

983 Wintsch, R.P., R. Christoffersen, and A.K. Kronenberg (1995), Fluid-rock weakening
984 of fault zones, *J. Geophys. Res.*, *100*(B7), 13021–13032,
985 doi:10.1029/1994JB02622.

986 Woodcock, N.H., and K. Mort (2008), Classification of fault breccias and related fault
987 rocks, *Geol. Mag.*, *145*(3), 434-440.

988 Wright, C.A. (1998), *Geology and Paleoseismology of the Central Alpine Fault New*
989 *Zealand*, MSc thesis. Dunedin, University of Otago.

990 Yang, H., L. Zhu, and E.S. Cochran (2011), Seismic structures of the Calico fault zone
991 inferred from local earthquake travel time modeling, *Geophys. J. Inter., 186,* 760-770.

992 *Figure captions*

993 **Figure 1**. Location map, Alpine Fault, South Island, New Zealand. (a) The Alpine Fault
994 forms the spine of the Southern Alps and marks the boundary between the Pacific and
995 Australian plates. The angular velocity describing the relative motion of the Pacific and
996 Australian plates can be resolved into ~39 mm/yr parallel to the Alpine Fault and 6-9
997 mm/yr perpendicular to it [*Beavan et al.*, 2010]. (b) DEM image of the central South
998 Island showing the location and strike of the Alpine Fault, which is subdivided into its
999 central and southern sections [*Barth et al.*, 2013]. Locations where fault gouge and/or
1000 cataclasite samples were collected for XRF and XRD analyses are starred in the figure
1001 (yellow star with bold outline), and fault orientation is given. At the Martyr River, only
1002 XRD analysis was conducted (yellow star). Additional exposures of thrust segment
1003 fault gouge not analyzed are shown as yellow circles; descriptions of these exposures
1004 were given by *Reed* [1964], *Wright* [1998], *Simpson* [1992] and *McClintock* [1999].
1005 Alpine Fault cataclasites were also described by *Sibson et al.* [1979], *Simpson et al.*
1006 [1994], *Norris and Cooper* [2007], *Toy* [2007], *Easterbrook* [2010], *Toy et al.* [2011],
1007 and *Scott* [2012].

1008 **Figure 2**. Hillshade view of the Gaunt Creek catchment derived from LiDAR data. The
1009 location of natural exposures of the faulted contact between (primarily) Pacific-plate
1010 derived cataclasites and Australian-plate derived cataclasites are shown with stars and
1011 the location of DFDP-1 drillholes are shown with crossed hexagons. Elevation of the
1012 contact is given in meters above seal level (asl). The Gaunt Creek catchment lies at the
1013 junction between dextral thrust and thrust segments of the fault [*Barth et al.*, 2012], and

1014 the strike of the fault changes from southwest to northeast across the creek. A 4-point
1015 solution constructed using the strike between the scarp and terrace exposures and the
1016 contact elevations yields an average fault dip of 28-30º.

1017 **Figure 3.** Schematic cross-sections of fault-related rocks comprising the DFDP-1A and
1018 DFDP-1B boreholes at Gaunt Creek with reference to outcrop geology. U2 denotes the
1019 uppermost documented occurrence of altered Unit 2 brown-green-black ultramylonites
1020 in each borehole. Colors on the cross-section indicate the relative proportions of each
1021 lithological unit recovered in the cored interval (see Key). Also pictured are core-scale
1022 examples of major lithological units identified in DFDP-1A and DFDP-1B. Each
1023 picture is a 180º core scan, except for 1B 144.75-144.95 m, which is a flat core scan.
1024 Colored boxes around each core-scale image correspond to the borehole depth interval
1025 from which they were sampled. Figure modified from *Sutherland et al.* [2012] and *Toy*
1026 *et al.* [2015].

1027 **Figure 4**. Plane-polarized light (PPL) optical microscope (OM) images of
1028 representative DFDP-1 fault rock lithologic units. Borehole depths are given on each
1029 image. 1A indicates DFDP-1A and 1B indicates DFDP-1B. (a) Unit 2 brown-green-
1030 black ultramylonite. In this OM image, the disjunctive cleavage spacing is < 1 mm and
1031 defined by fine-grained phyllosilicates and opaques (dashed white lines). Unit 2 is
1032 commonly interlayered with Unit 3 and a typical contact is shown (solid white line).
1033 (b) Abundant e-twinned calcite in a Unit 4 foliated cataclasite. A planar foliation
1034 appears at the bottom of the images, and it is defined by fine-grained opaques, chlorite,
1035 muscovite, plagioclase, potassium feldspar, and quartz. (c) Unit 4 foliated cataclasite
1036 with boudinaged porphyroclasts of quartz, plagioclase, and calcite. Chlorite commonly
1037 occurs in zones of dilatation. Opaques, muscovite, chlorite, and rare epidote, form the
1038 foliation (dashed white lines). (d) Unit 4 foliated cataclasite with anastomosing foliation

1039 defined by chlorite and muscovite with accessory graphite (dashed white lines). (e) Unit
1040 6a lower cataclasite derived from a granitoid protolith. Intragranular fracture in center
1041 clast is filled with chlorite; matrix is composed of ultrafine-grained chlorite, muscovite,
1042 quartz, and plagioclase. (f) Unit 6d lower cataclasite with an anastomosing foliation of
1043 ribbon quartz and muscovite grains derived from a gneissic protolith (cf. Figure 6f)
1044 (dashed white lines). (g) Gouge clast in lower DFDP-1B Unit 5 gouge. Note
1045 concentration of phyllosilicates along margins of gouge clast (arrows). (h) Unit 7
1046 breccia clasts have a mylonitic foliation (dashed white lines) defined by opaques and
1047 elongated plagioclase and quartz; accessory graphite and apatite are also common.

1048 **Figure 5.** Scanning electron microscope (SEM) backscattered electron (BSE) images
1049 of representative DFDP-1 fault rock lithologic units. All thin-sections are not oriented.
1050 Borehole depths are given on each image. 1A indicates DFDP-1A and 1B indicates
1051 DFDP-1B. For all microstructures: Qtz is quartz; KSp is potassium feldspar; Pl is
1052 plagioclase; Ms is muscovite; Cl is chlorite; Bt is biotite; Sm is smectite; Cal is calcite;
1053 Op is opaques; Ilm is ilmenite; Ttn is titanite; Ep is epidote; Zrn is zircon. (a) Unit 2
1054 brown-green-black ultramylonite. A ~mm-spaced disjunctive cleavage appears as fine-
1055 grained, parallel grains of plagioclase (oligoclase) and muscovite with accessory
1056 titanite. Shear sense given by stair-stepped quartz clast. (b) Unit 2 brown-green-black
1057 ultramylonite with an anastomosing network of cataclasite-filled fractures, which yield
1058 a shear sense. (c) Unit 3 upper unfoliated cataclasite composed of angular clasts of
1059 altered Unit 2 cemented with calcite (similar to the mosaic breccia of *Woodcock and*
1060 *Mort* [2008]). (d) Typical Unit 3 upper unfoliated cataclasite random-fabric matrix
1061 composed of altered plagioclase porphyroclasts, quartz, and calcite with embayed
1062 margins. (e) Unit 4 upper foliated cataclasite which has a Unit 2 protolith identical to
1063 image (a). Note strongly corroded clast margins, enhanced porosity, and ultrafine-

grained matrix chlorite and muscovite. (f) Unit 4 upper foliated cataclasite with foliation defined by comminuted grains. Protolith appears similar to Unit 2 in image (a), but alteration to chlorite and white mica is ubiquitous. Note also the presence of potassium feldspar, which is not present in Unit 2. (g) Unit 4 upper foliated cataclasite with foliation defined by aligned phyllosilicates that appear to link in an anastomosing network similar to an S-C'' shear fabric. (h) A foliated portion of a Unit 6d lower cataclasite. The foliation is defined by ~100 μm-long aligned muscovite grains sourced from a gneissic protolith. Calcite is sparse.

Figure 6. Scanning electron microscope (SEM) backscattered electron (BSE) images of representative DFDP-1 fault rock lithologic units. Borehole depths are given on each image. 1A indicates DFDP-1A and 1B indicates DFDP-1B. (a) Unit 5 gouge containing reworked gouge clasts (gc). Several types of gouges occur within the central gouge clast. Other prominent clast types include variably altered Unit 2 ultramylonite, calcite, and potassium feldspar with inclusions of quartz and titanite. (b) Boudinaged and faulted hairline calcite-veins in a more competent Unit 5 gouge. (c) A boundary between a quartz-calcite clast in the Unit 6b lower foliated cataclasite and a Unit 5 gouge. Multiple fractures are sealed by calcite (arrows). (d) Gouge clast within a Unit 5 gouge. Calcite occurs as crenulated vein fragments and embayed clasts (arrows). Bright clast is coated in skeletal titanite. (e) Unit 6d lower cataclasite clasts derived from a granitoid protolith. Central clast is potassium feldspar with myrmekitic intergrowths of quartz in plagioclase. (f) Unit 6d lower cataclasite clast derived from a gneissic protolith. Note large ribbon quartz grains and muscovite, which is fracturing along cleavage planes and being incorporated into the matrix. (g) Unit 6d lower cataclasite matrix with rare calcite cement, which is more common near PSZ gouges. Overall, Unit 6 cataclasites are more porous than Unit 3 and 4 upper cataclasites (pores

1089 are black in BSE images). (h) Augen-bearing mylonite in the Unit 7 breccia. Foliation
1090 is defined by elongated quartz, chlorite, and plagioclase.

1091 **Figure 7.** Variations in relative major element oxide abundance, given as wt. %, with
1092 depth in DFDP-1A. A semi-transparent gray line marks the depth of the Unit 5 PSZ
1093 gouge (labeled PSZ), which is the contact between hanging wall lithologic units (Units
1094 1-5) and footwall gravels (Unit 8). See text for details.

1095 **Figure 8.** Variations in relative major element oxide abundance, given as wt. %, with
1096 depth in DFDP-1B. A semi-transparent gray line marks the depth of the Unit 5 PSZ-1
1097 gouge (labeled PSZ-1), which is the contact between hanging wall lithologic units
1098 (Units 1-5) and footwall lithologic units (Units 6 and 7). Another semi-transparent gray
1099 line marks the depth of the Unit 5 PSZ-2 gouge (labeled PSZ-2), which is the contact
1100 between Unit 6 footwall cataclasites and Unit 7 footwall breccia. See text for details.

1101 **Figure 9.** Ternary plots of variations in major element geochemistry for samples
1102 analyzed from DFDP-1A and DFDP-1B. All units are wt. %. Hanging wall fault-related
1103 rocks are grouped: Units 1 and 2 mylonites (green down triangles), and Units 3 and 4
1104 cataclasites (yellow up triangles). Unit 5 gouges (DFDP-1A PSZ, DFDP-1B PSZ-1 and
1105 PSZ-2) are grouped together (red diamonds). Footwall lithologic units are: Unit 6
1106 footwall cataclasites (green squares), Unit 7 footwall breccia (grey squares), and Unit
1107 8 footwall gravels (orange squares). Also plotted are average hanging wall protolith,
1108 Otago Schist (n=38), Alpine Schist (n=25), Caples Schist (n=20), and metabasite
1109 (n=18) compositions from *Pitcairn* [2004]. Average footwall protolith, Karamea Suite
1110 granitoids, Greenland Group greywacke and argillite, compositions were calculated
1111 from data in PETLAB, most of which were published in *Nathan* [1976, 1998], *Roser et*
1112 *al.* [1995], *Tulloch and Palmer* [1990], and *Tulloch et al.* (2009) (results downloaded

1113 from PETLAB http://pet.gns.cri.nz). Purple shaded regions around each footwall
1114 protolith composition represent ±1σ. (a) A ternary plot of Al_2O_3-Na_2O+K_2O-
1115 MgO+Fe_2O_3 variations. Hanging wall lithologic units follow a trend between Otago
1116 Schist/Alpine Schist and metabasite protolith compositions; the hanging wall
1117 cataclasites are relatively more enriched in MgO+Fe_2O_3. Footwall lithologic units
1118 follow a trend between Unit 7 footwall breccia and Karamea Suite protolith, but some
1119 Unit 6 cataclasites are relatively enriched in Al_2O_3-Na_2O+K_2O. (b) A ternary plot of
1120 Al_2O_3-CaO-MgO+Fe_2O_3 variations. Hanging wall lithlogic units do not follow a trend
1121 between protolith compositions, but rather follow a trend from Otago Schist/Alpine
1122 Schist protolith composition towards relative CaO-enrichment. A single footwall
1123 catclasite, from DFDP-1B 143.9 m immediate above PSZ-2, has a higher amount of
1124 CaO. Footwall lithologic units follow a trend between Unit 7 footwall
1125 breccia/Greenland Group argillite and Karamea Suite protolith, but some Unit 6
1126 cataclasites have relatively more Al_2O_3.

1127 **Figure 10**. During exhumation from subgreenschist facies temperatures and
1128 pressures, Alpine Fault cataclasites and gouges have undergone multiple phases of
1129 alteration. Following *Warr and Cox* [2001] and *Chamberlain et al.* [1999], primary
1130 non-oxidized and oxidized alteration reactions are outlined in the figure. K-feldspar is
1131 not present in Alpine or Otago Schist protoliths, but it is observed in DFDP-1A and
1132 DFDP-1B lithologic units, particularly below PSZ-2 in DFDP-1B. See text for more
1133 details.

1134 **Figure 11.** Plate boundary cross-section and schematic model of earthquake cycle
1135 processes occurring on the Alpine Fault at Gaunt Creek. (a) There are several fluid
1136 sources within the Alpine Fault Zone, including mantle (green arrows) and
1137 metamorphic (yellow arrows) fluids, but meteoric water (blue arrows) is volumetrically

1138 dominant within the brittle crust [modified from *Menzies et al.*, 2016]. (b-d) Diagrams
1139 illustrating key processes that affect fault core permeability and, potentially, rheology.
1140 The Alpine Fault forms an impermeable barrier throughout the earthquake cycle (bold
1141 diagonal line). (b) Immediately after an earthquake, hanging wall and footwall
1142 permeability is relatively high due to off-fault fractures (i.e., damage). Damage is likely
1143 greater in the hanging wall [e.g., *Ma and Beroza*, 2008]. Short black lines denote open
1144 fractures; open purple circles represent phyllosilicates. (c) As meteoric fluids pond
1145 against the impermeable fault, carbonate (calcite) precipitates and seals open fractures
1146 during the interseismic period. The footwall is isolated from calcite-rich meteoric
1147 fluids. Short magenta lines denote calcite-sealed fractures. (d) During the late-
1148 interseismic period, open fractures near the Alpine Fault are sealed with calcite.
1149 Phyllosilicate nucleation and growth occurs more slowly; phyllosilicates within the
1150 fault core likely formed over multiple earthquake cycles [e.g., *Meunier*, 2005].

1151 *Table captions*

1152 **Table 1** Description of lithologic units recovered in DFDP-1 modified from *Toy et al.*
1153 [2015]. Grain size describes matrix grains and clasts and/or porphyroclasts.
1154 Abbreviations are: Qtz is quartz, Pl is plagioclase (primarily oligoclase and/or albite),
1155 Bt is biotite, Ms is muscovite, Cal is calcite, Am is amphibole, Ep is epidote, Cl is
1156 chlorite, Ilm is ilmenite, Ttn is titanite, Sme is smectite, Mnt is montmorillonite, Kln is
1157 kaolinite, Gt is goethite, Mn is manganese oxide-hydroxide, Zrn is zircon, Ap is apatite,
1158 Gr is graphite.

1159 **Table 2** Qualitative X-ray diffraction data for selected samples recovered from DFDP-
1160 1A and DFDP-1B core. Mineralogy of plagioclase and feldspar could not be discerned.
1161 (*) denotes that sample 1a_66_5 may contain both chlorite and biotite. No samples

1162 were available for the core interval below PSZ-2 in DFDP-1B, and those samples were
1163 analyzed with quantitative XRD (Table 3). For DFDP-1B 128.80m, “w” and “gw” stand
1164 for white and green-white, the color of the specific sample.

1165 **Table 3** Quantitative X-ray diffraction data for selected samples recovered from DFDP-
1166 1B core. Mineralogy of plagioclase and feldspar could not be discerned. The
1167 dioctahedral smectite present is montmorillonite-15Å. White mica denotes muscovite-
1168 2M1, but illite-2M1 may also be present. Chlorite is clinochlore-1MIIB, and the
1169 amphibole is actinolite. Amorphous phases were not identified and results are
1170 normalized to 100%. All samples from the DFDP-1B borehole, latitude/longitude co-
1171 ordinates 43.3141ºS/170.3259ºE.

1172 **Table 4** Quantitative X-ray diffraction data for cataclasites and fault gouges collected
1173 at localities along strike of the central and southern Alpine Fault. (*) Sample 34119 was
1174 from a weathered block and was not a separate from sample 34104. Lithologic units are
1175 described in the text. Abbreviations are: fol, foliations present; uccl, the most highly
1176 comminuted, striated gouge that marks the HW/FW contact; rim, a foliated cataclasite
1177 present on the rim of a serpentinite pod. WR denotes whole rock, and < 2 μm denotes
1178 clay-sized fraction. Mineralogy of plagioclase and feldspar could not be discerned. The
1179 dioctahedral smectite present is montmorillonite-15Å. White mica denotes muscovite-
1180 2M1, but illite-2M1 may also be present. Chlorite is clinochlore-1MIIB, the serpentine
1181 is lizardite-1M, and the amphibole is actinolite. There was insufficient kaolin present
1182 to discern kaolinite from dickite. Amorphous phases were not identified, and results are
1183 normalized to 100%. Location latitude/longitude co-ordinates are: Little Man River
1184 43.1400ºS/170.2818ºE; Gaunt Creek Terrace and Gaunt Creek Scarp
1185 43.3141ºS/170.3259ºE; Stoney Creek 43.2290ºS/170.1239ºE; Waikukupa River
1186 43.2622ºS/170.0490ºE; Robinson Creek 43.4956ºS/169.1350ºE; Martyr River

1187 44.1326ºS/168.5536ºE; McKenzie Creek 44.3599ºS/168.1390ºE; Hokuri Creek
1188 44.4062ºS/168.0648ºE.

1189 **Table 5** Major element geochemistry of DFDP-1A samples from XRF and ICP-AES
1190 analysis. All values are in wt. %. Fe_2O_3t denotes total Fe_2O_3. NA denotes not analyzed.
1191 All "DFDP" samples analyzed with ICP-AES; instrument precision for this method is
1192 ±0.02 wt.%. Analytical error for this method varies with major element oxide and
1193 sample abundance of major element oxide. Repeat standard analyses yield the
1194 following maximum analytical errors: SiO_2 ±2.20%; TiO_2 ±1.55%; Al_2O_3 ±2.68%;
1195 Fe_2O_3 ±2.52%; MnO ±0.01%; MgO ±1.60%; CaO ±5.44%; Na_2O ±9.00%; K_2O ±
1196 2.53%. Other oxide abundances (wt. %) were within instrument precision with
1197 analytical errors up to 100%. "RW_XRF" samples were analyzed with XRF; instrument
1198 precision for this method was not available. Repeat standard analyses yield the
1199 following maximum analytical errors: SiO_2 ±0.20%; TiO_2 ±0.44%; Al_2O_3 ±0.34%;
1200 Fe_2O_3 ±0.21%; MnO ±10.88%; MgO ±2.32%; CaO ±0.44%; Na_2O ±8.32%; K_2O ±
1201 0.60%. A maximum LOI analytical error ±11.55% was calculated from repeat standard
1202 analyses provided by ALS Minerals. LOI, listed as percentage by weight, is a measure
1203 of the volatile content of the samples, and this measurement includes the weight loss
1204 due to both dehydration and decarbonation reactions

1205 **Table 6** Major element geochemistry of DFDP-1B samples from ICP-AES analysis.
1206 All values are in wt. %. Fe_2O_3t denotes total Fe_2O_3. NSS denotes not sufficient sample.
1207 Instrument precision and analytical error as reported in the Table 5 caption.

1208 **Table 7** Balanced alteration reactions and solid volume changes associated with each
1209 reaction. All reactions balanced assuming simplified end-member mineral formula.
1210 Calculated solid volume changes assume the product SiO_2 precipitates as quartz;

however, SiO_2 can leave the reaction site as an aqueous species. Iron may be present in clinochlore and montmorillonite minerals, but reactions are balanced assuming only octahedral magnesium cations. Reactions 1-8 from *Wintsch and Yeh* [2013]. End member formulas from *Holland and Powell* [1998]; end member illite formula from *Deer et al.* [1992]. Note the density of phyllosilicate minerals can vary with cation ratio and interlayer hydration state [e.g., *Totten et al.*, 2002].

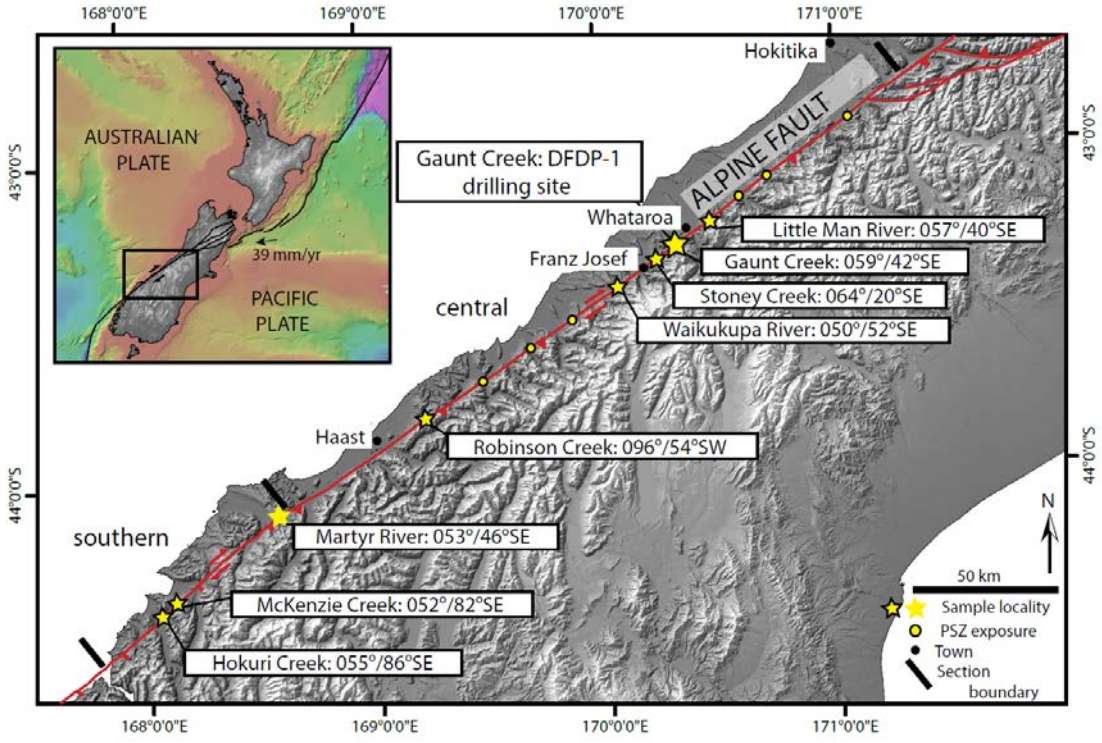

Figure 1

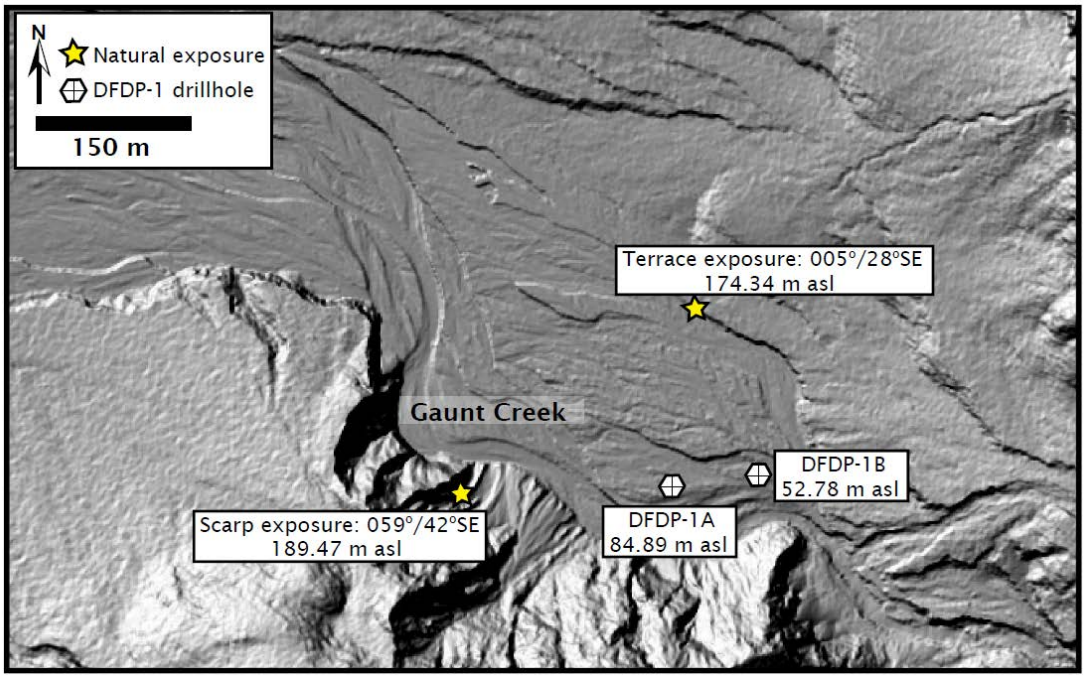

1219

1220 Figure 2

1221

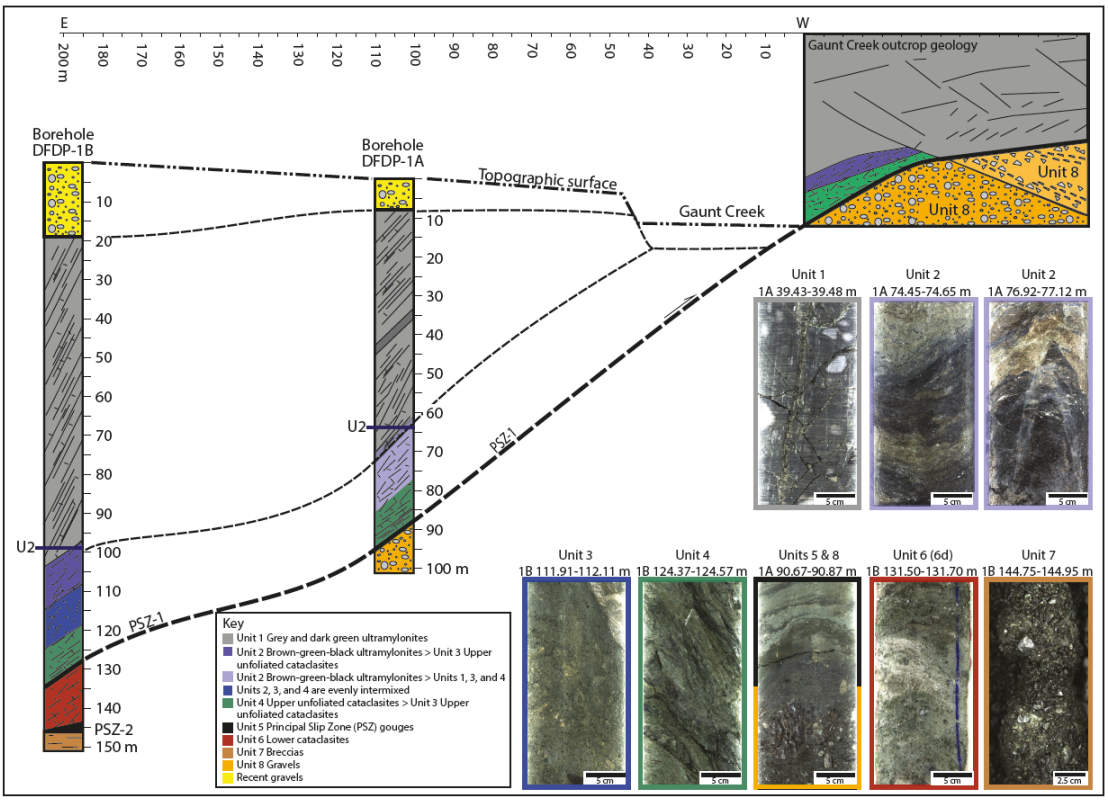

1222

1223 Figure 3

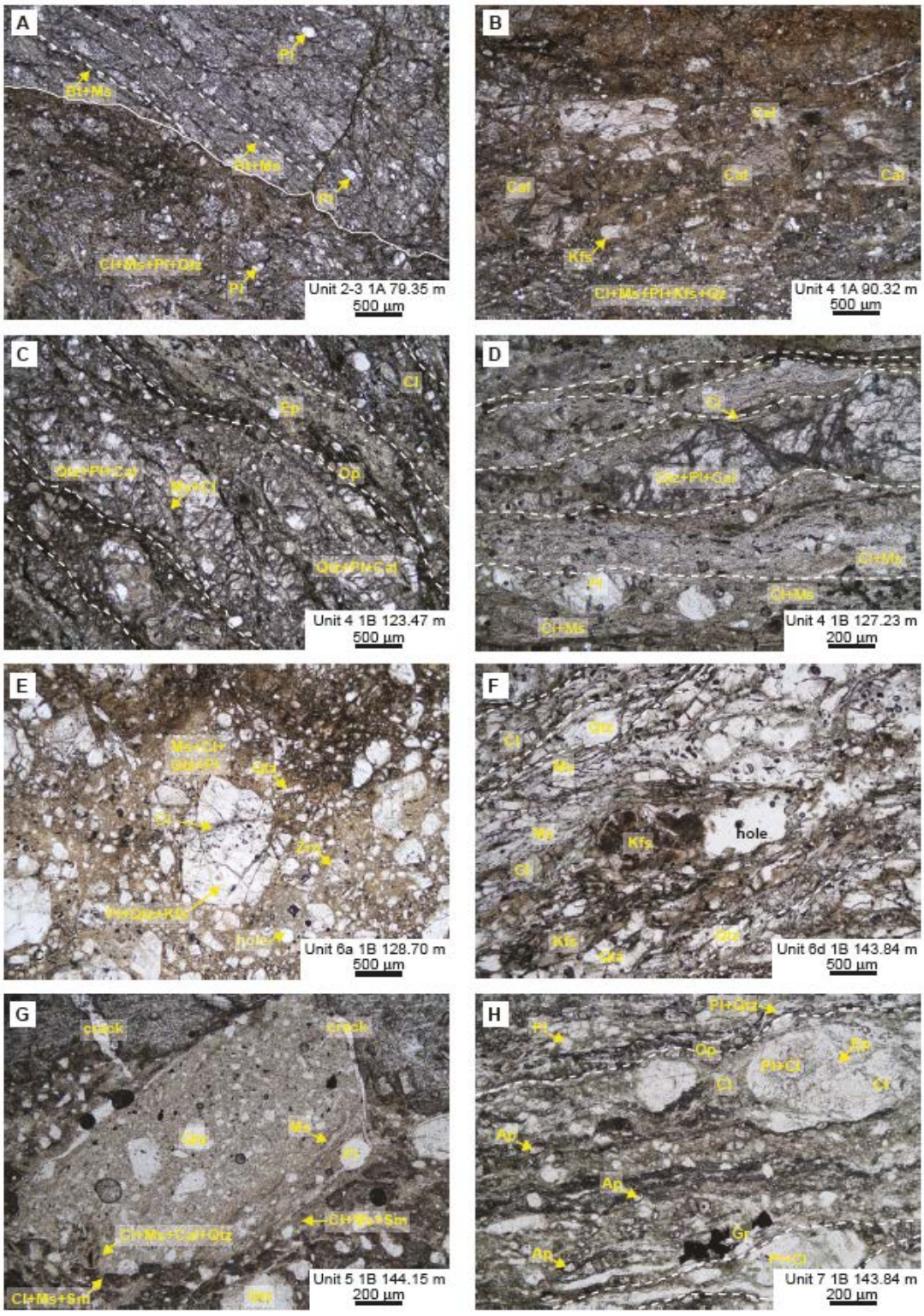

1224

1225 Figure 4

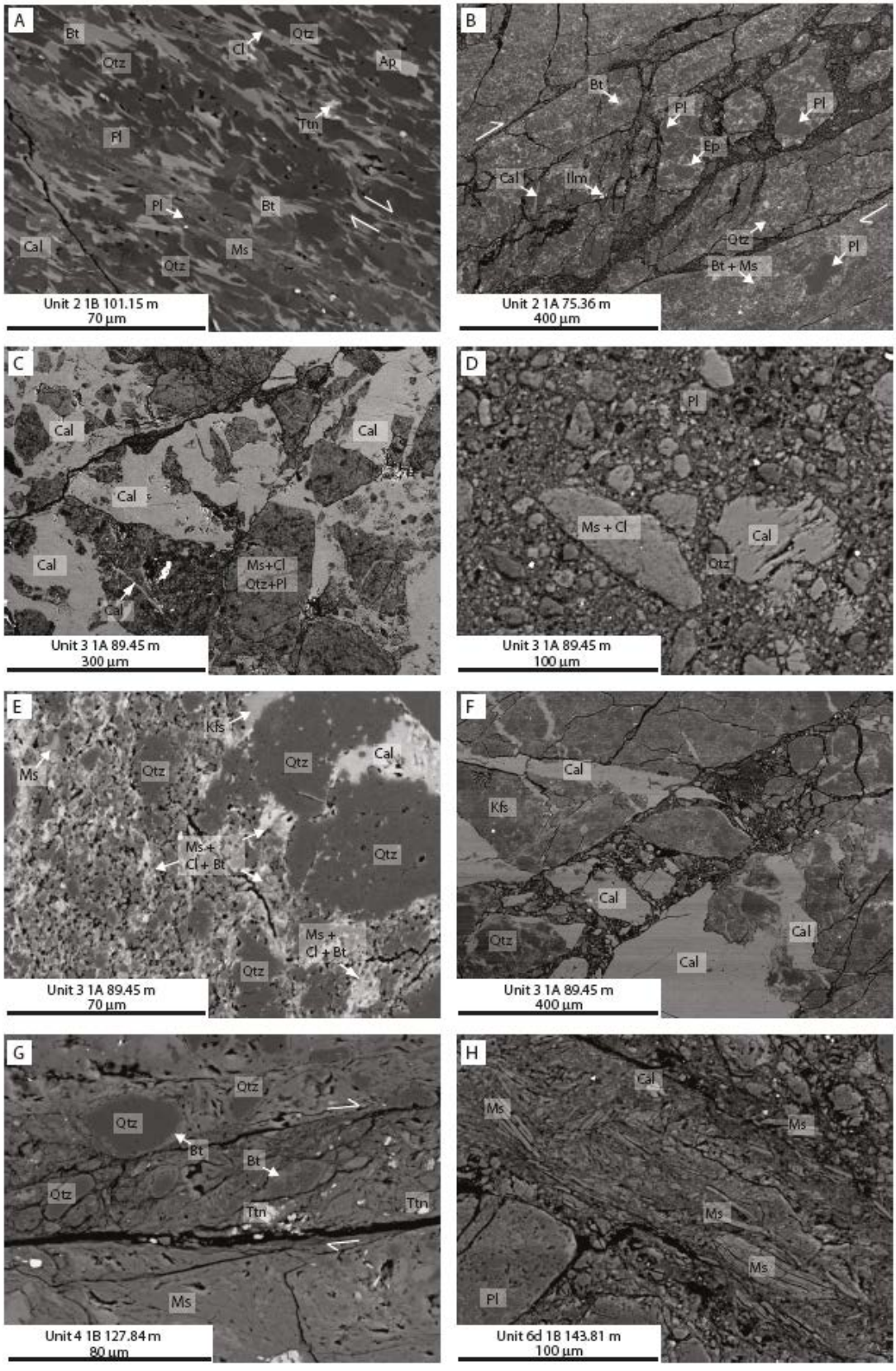

1226

1227 Figure 5

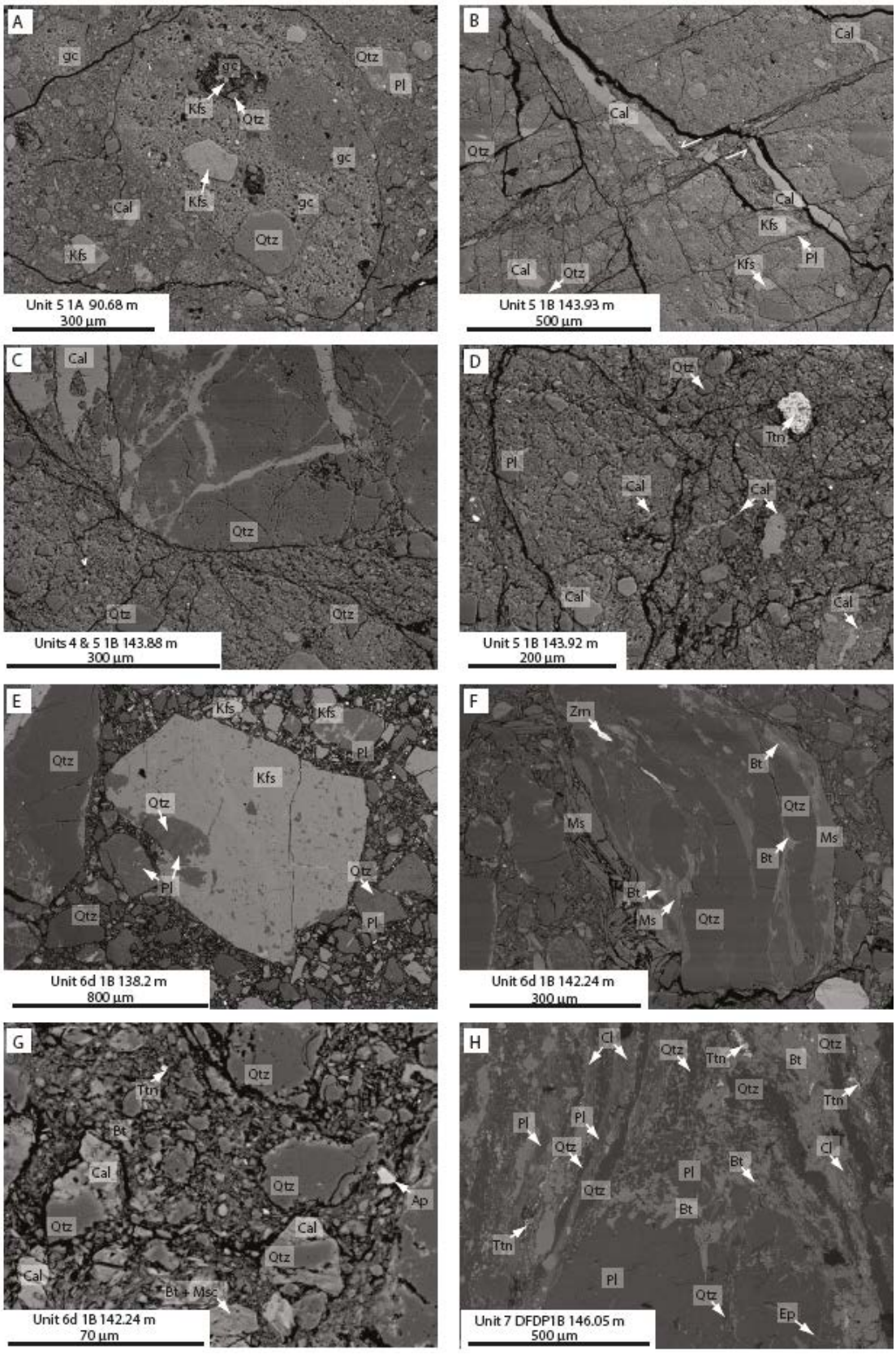

1228

1229 Figure 6

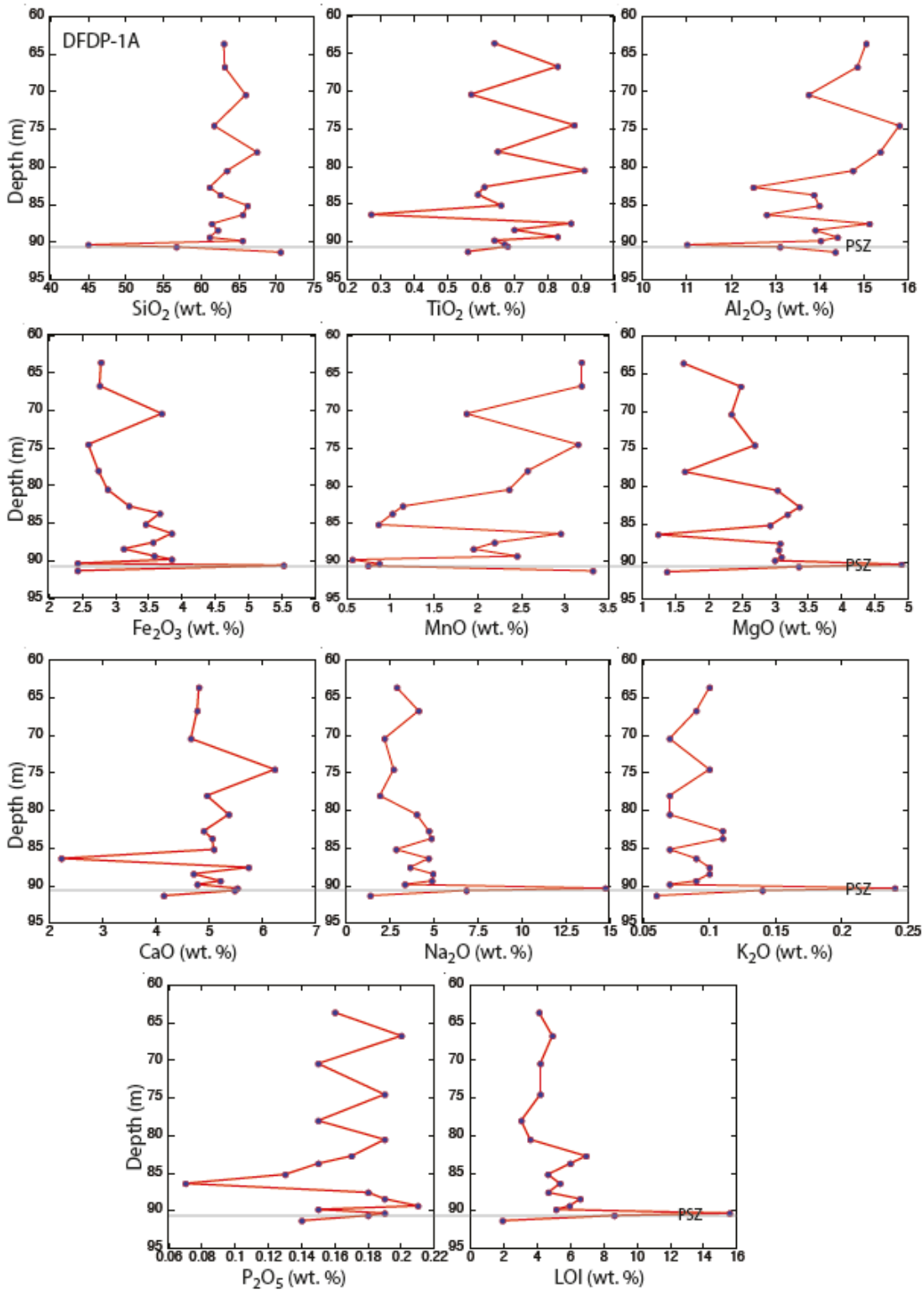

1230

1231 Figure 7

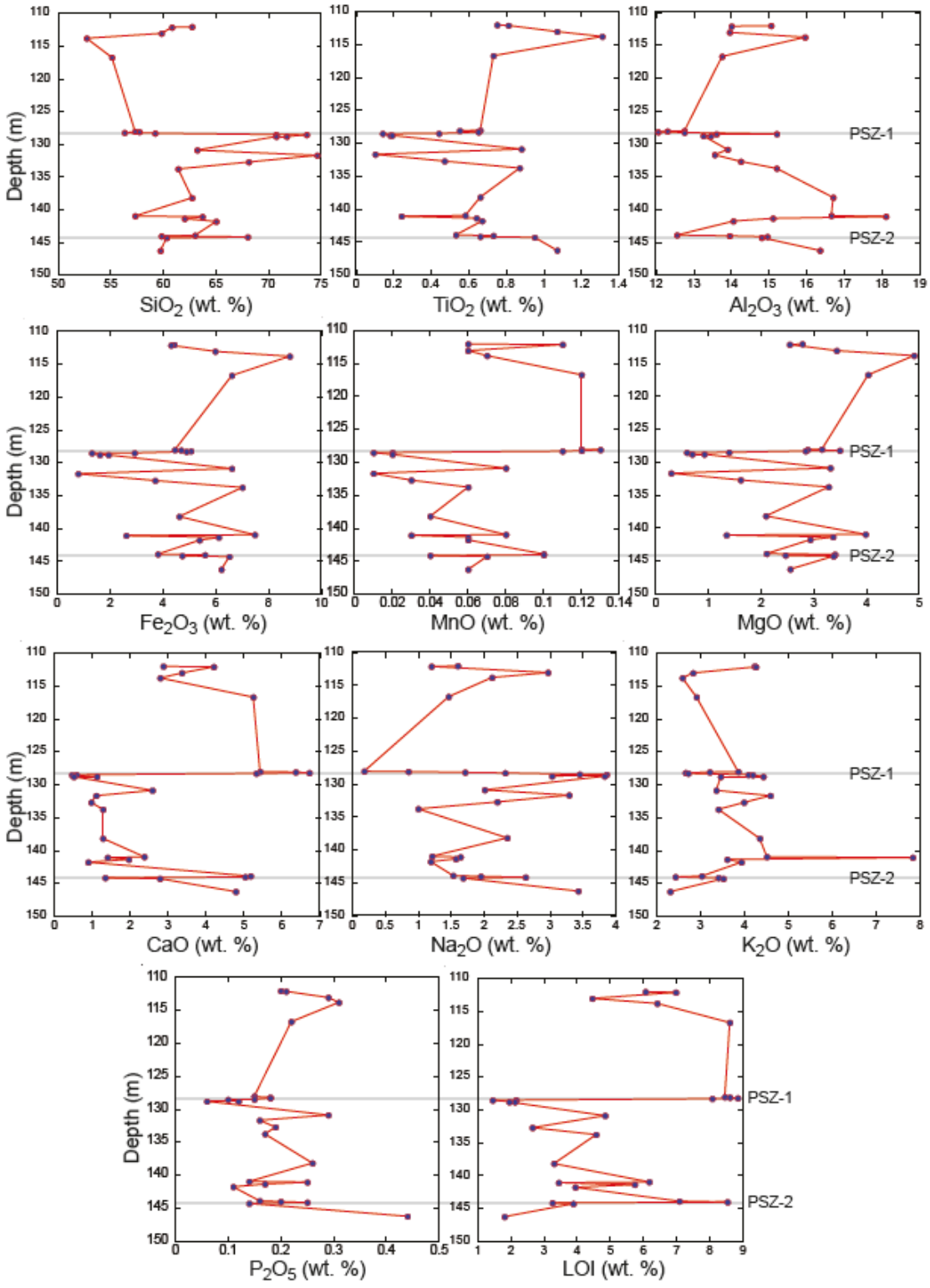

1232

1233 Figure 8

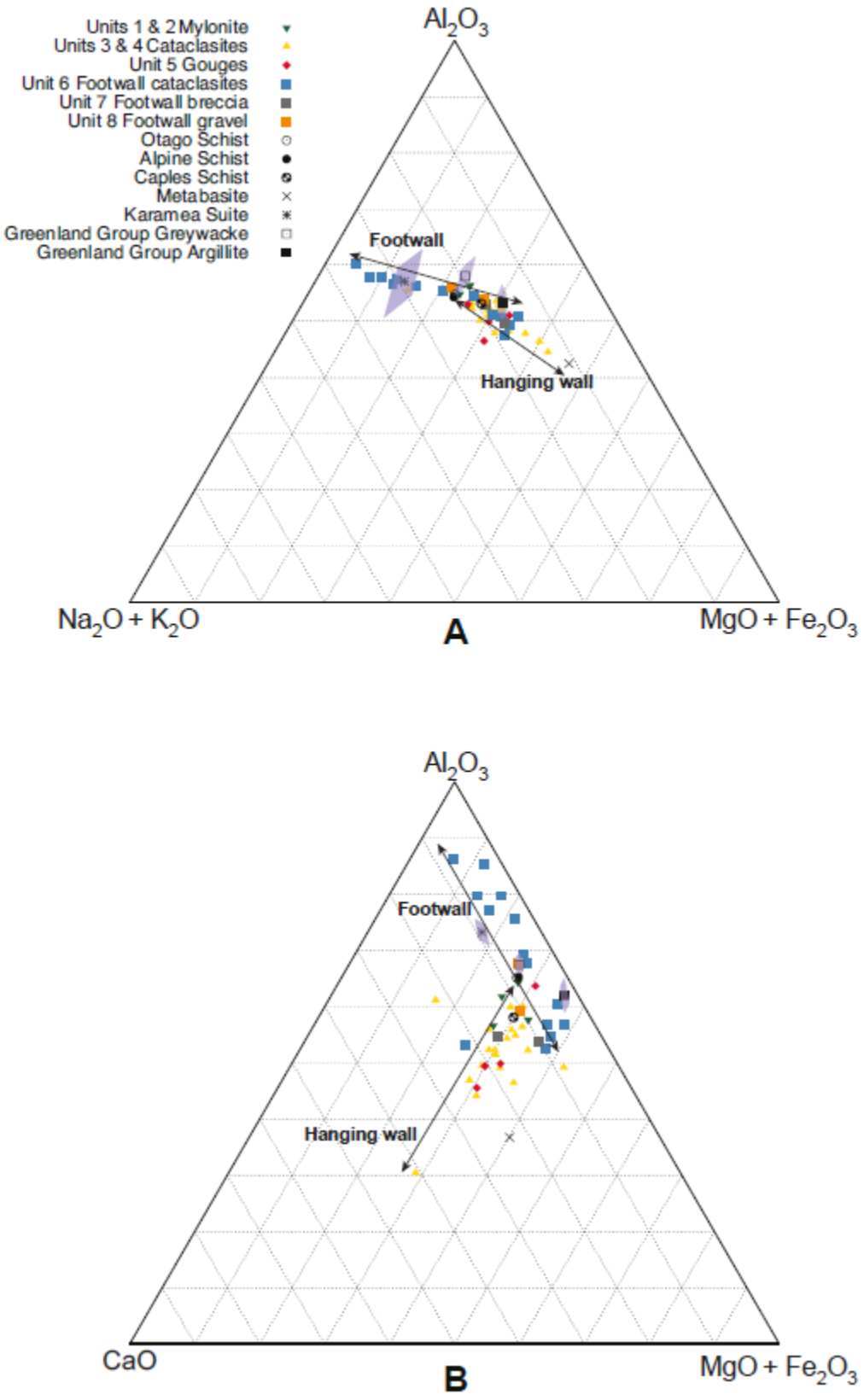

1234

1235 Figure 9

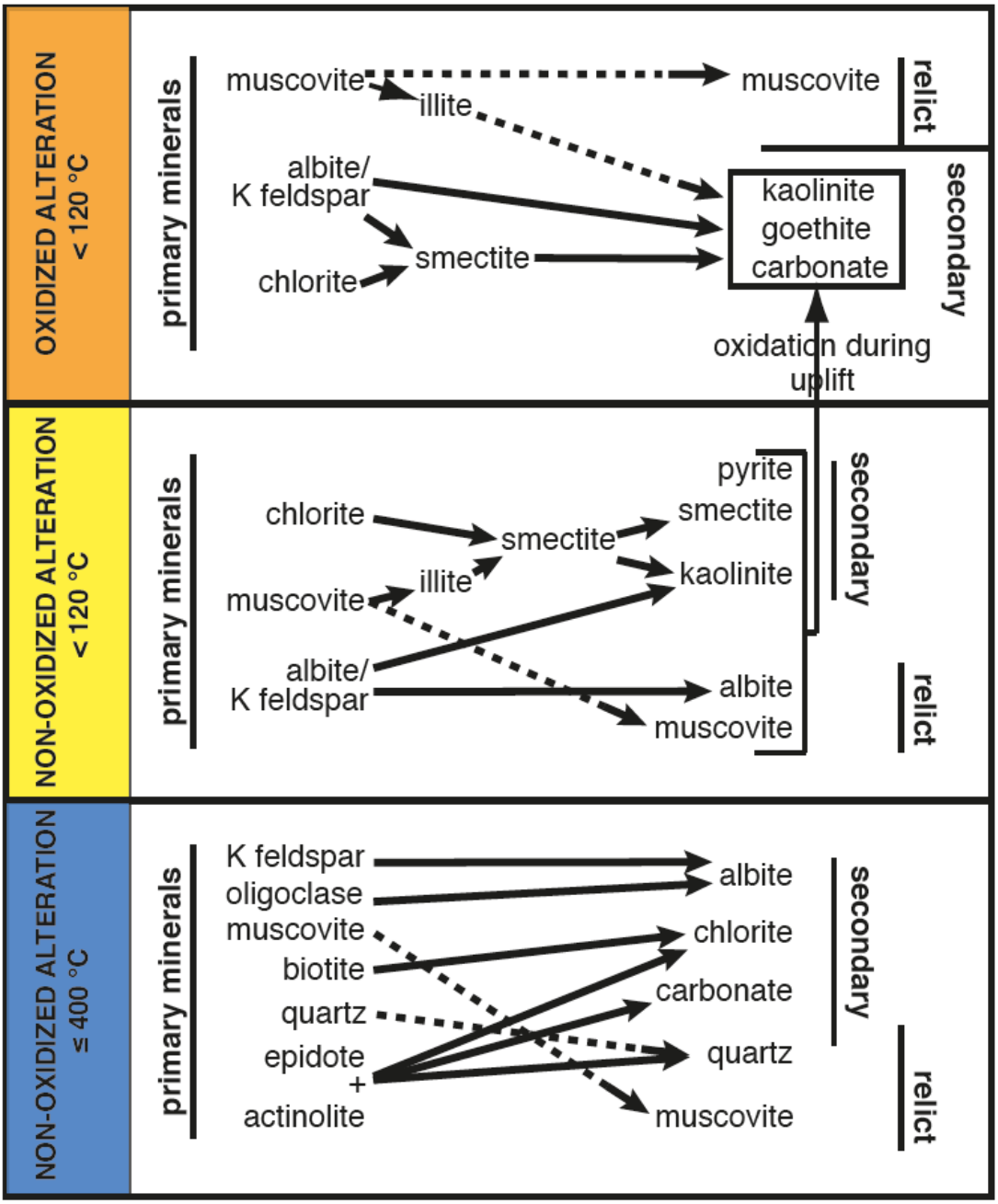

1236

1237 Figure 10

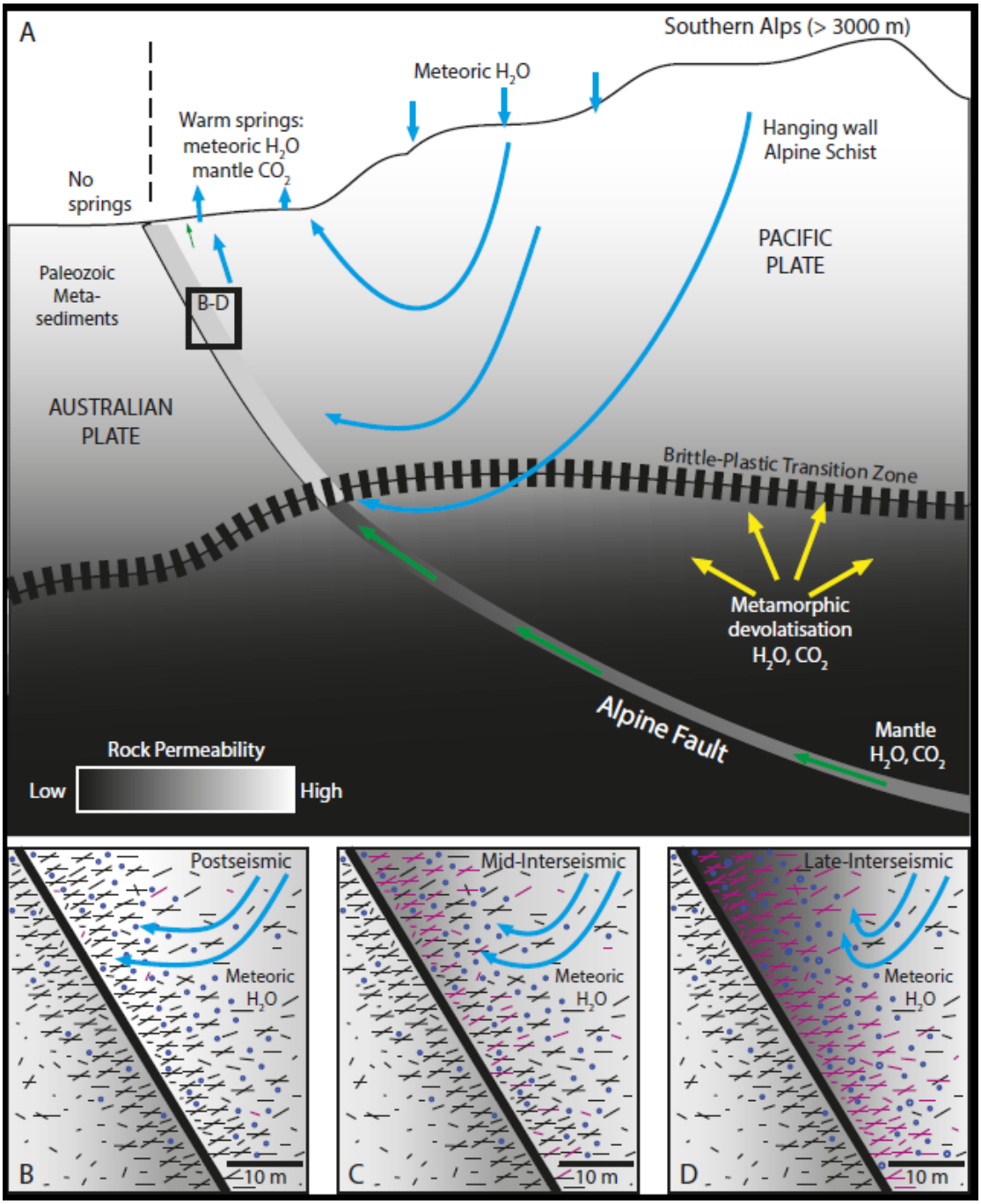
A
Southern Alps (> 3000 m)
Meteoric H_2O
Warm springs:
meteoric H_2O
mantle CO_2
No
springs
Hanging wall
Alpine Schist
PACIFIC
PLATE
Paleozoic
Meta-
sediments
B-D
AUSTRALIAN
PLATE
Brittle-Plastic Transition Zone
Metamorphic
devolatisation
H_2O, CO_2
Alpine Fault
Mantle
H_2O, CO_2
Rock Permeability
Low
High
Postseismic
Meteoric
H_2O
10 m
B
Mid-Interseismic
Meteoric
H_2O
10 m
C
Late-Interseismic
Meteoric
H_2O
10 m
D

Figure 10

1244

Table 1. Abbreviated description of lithologic units after *Toy et al.* [2015].

Lithologic Unit	Name	Description	Dominant microstructure(s)	Grain size (mm)	Mineralogy
Unit 1	Grey and dark green ultramylonites	Planar-foliated mylonite to ultramylonite	Segregations of Qtz+Pl and Ms+Bt±Ep±Chl with locally abundant Pl-augen trains, mm-spaced continous foliation	>0.03 to >1	Qtz+Pl+Bt+Ms±Cal±Am±Ep±Cl±Ilm±Ttn
Unit 2	Brown-green-black ultramylonites	Planar-foliated ultramylonite	Indistinct mm-spaced foliation defined by opaque seams and parallel mica grains which form a locally dilatant disjunctive cleavage; Pl-augen common	<0.05 to <0.2	Qtz+Pl+Bt+Ms+Cl±Cal±Ep±Am±Ilm±Ttn
Unit 3	Upper unfoliated cataclasites	Unfoliated cataclasites derived from Units 1 and 2	Angular clasts of Units 1 and 2 in a variably calcite-cemented ultrafine-grained matrix (<0.1 mm-grains)	<0.01 to <0.1 with <100 clasts	Qtz+Pl+Bt+Ms+Cl±Cal±Ep±Am±Ilm±Ttn
Unit 4	Upper foliated cataclasites	Foliated cataclasites derived from Units 1-3	Foliation defined by micro-shears, anastamosing seams of opaques, and/or locally aligned phyllosilicates; e-twinned veins and clasts of calcite	<0.01 to <0.1	Qtz+Pl+Ms+Cl+Cal±Bt±Ep±Am±Ilm±Ttn

Unit 5	Gouges	Cemented to uncemented gouges with variable mineralogy	Predominantly random fabric with rare locally aligned phyllosilicates; e-twinned calcite clasts; gouge and cataclasite clasts common	<0.001 to <0.01	Qtz+Pl+Ms+Cl+Cal±Ksp±Sme(Mnt)±Kln±Gt±Mn±Ilm±Ttn ±Zrn±Ap
Unit 6	Lower cataclasites-divided into 4 subunits	6a- white to cream-coloured ccl with granitoid and gneissic clasts; 6b- greenish grey foliated protocataclasite; 6c- greenish grey to black ultracataclasite to gouge with gneiss, Qtz-Pl-Fsp, and rare mylonite clasts; 6d- a mixture of 6a-6c.	6a- random fabric, granitoid clasts contain myrmekite and antiperthite textures, gneissic clasts contain ribbon Qtz; 6b - foliations comprise muscovite and chlorite; 6c- random fabric; 6d - interlayered mixture of 6a-6c containing numerous micro- to meso-scale faults	<<0.03 to >>0.1	Qtz+Ksp+Pl+Ms±Bt±Cl±Zrn±Ap±Ttn
Unit 7	Breccias	Protoccl to breccia composed of black myl-gneiss clasts	Remnant mylonitic-gneissic foliation with Pl-augen or Qtz segregations; phyllosilicate foliations wrap porphyroclasts	<1 to >10	Qtz+Ksp+Pl+Ms+Bt+Cl+Ep+Ap+Ttn+Gr
Unit 8	Gravels	Quaternary gravels composed primarily of Alpine Schist clasts	Locally imbricated	0.25 to >10	Qtz+Pl+Bt+Ms±Cal±Am±Ep±Cl±Ilm±Ttn

1245

1246

1247

Table 2. Qualitative X-ray diffraction data for DFDP-1 samples.

Hole depth (m)	Lithology	Quartz	K Feldspar	Plagioclase	Muscovite	Biotite	Chlorite	Calcite	Ankerite	Spinel	Epidote
63.6	1	X		X	X		X	X			
66.7	2	X		X		X	X	X			
70.6	3	X		X	X		X				
74.5	4	X		X	X		X	X			
82.7	4	X		X	X		X	X			
86.35	4	X	X	X	X		X	X			
88.4	4	X		X	X		X	X			
89.34	4	X	X	X	X		X	X			
90.32	4	X	X	X	X		X	X			
90.62	5	X	X	X	X		X	X			
91.3	8	X		X	X	X	X				
112.12	3	X	X	X	X		X	X	X		
113.81	3	X		X	X		X				
116.72	3	X		X	X		X	X			
128.04	5	X			X		X	X		X	
128.09	5	X		X	X		X	X			
128.22	5	X		X	X		X	X			
128.5	6	X	X	X	X		X				
128.53	6	X	X	X	X		X				
128.80 w	6	X	X	X	X		X				
128.80 wg	6	X	X	X	X		X				
128.81	6	X	X	X	X		X				
130.88	6	X	X	X	X		X	X			

131.68	6	X	X	X	X		X				X		
132.7	6	X	X	X	X		X				X		
133.75	6	X	X	X	X		X						
140.96	6	X	X	X	X		X	X		X			
141.07	6	X	X	X	X		X						
141.77	6	X	X	X	X		X				X		
141.9	6	X		X	X		X			X			
143.9	6	X		X	X		X	X					
144.02	7	X	X	X	X		X	X					
144.145	7	X	X	X	X		X						
144.28	7	X		X	X	X	X						

Table 3. Quantitative XRD data for DFDP-1B samples reported as modal abundance (%).

Sample	Hole Depth (m)	Lithology	Quartz	K feldspar	Plagioclase	Calcite	Kaolin	Smectite	White mica	Chlorite	Amphibole	Pyrite	Total
36184	128	5 (PSZ1)	25	4	25	9	6	18	12		1	<1	99
36185	143.9	6/5 transition	41	<1	14	10			30	5		<1	100
36186	144.02	5 (PSZ2)	29	3	24	8		18	17	1		<1	100
36187	144.14	5 (PSZ2)	36	4	23	5		15	15	2		<1	100
36188	144.15	5/7 transition	33	2	36				26	3		<1	100
36189	144.28	7	34	2	35	2				4		<1	77

Table 4. Quantitative XRD data for selected localities along-strike of the Alpine Fault reported as modal abundance (%).

Sample	Location	Lithology	Fraction	Quartz	K feldspar	Plagioclase	Calcite	Mg-Calcite	Ankerite	Kaolin	Smectite	White mica	Chlorite	Serpentine	Talc	Amphibole	Pyrite	Laumontite	Total
36959	Little Man R.	5	WR	18	3	33	10			6	20	10							100
34103	Gaunt Ck Terrace	5	WR	35	<1	17	6					32	9						99
3410 3_2	Gaunt Ck Terrace	5	< 2 µm	5		3						50	42						100
35067	Gaunt Ck Scarp	3	WR	49	10	19	2		12	8				<1					100
34113	Gaunt Ck Scarp	3	< 2 µm	<1								68	32						100
34112	Gaunt Ck Scarp	4fol	< 2 µm	9	3	27	2			4	36	16	2						99
34104	Gaunt Ck Scarp	5	WR	30	6	26	7	1		6	7	17							100
3411 9*	Gaunt Ck Scarp	5	< 2 µm	8		16					29	17	29						99
34105	Gaunt Ck Scarp	5uccl	WR	25	5	20	5			7	14	16		8					100
34117	Stoney Ck	3	< 2 µm	4	<1	7	8					41	40						100
35363	Waikukupa R	4	WR	35	33	6			1			6	19				<1	<1	100
34114	Waikukupa R	4	< 2 µm	4		19	2					21	51					2	99
34106	Waikukupa R	5	WR	28		26	25		<1			14	5			2	<1		100
34118	Waikukupa R	5	< 2 µm	8	<1	10	10				24	26	22						100
34107	Waikukupa R	5uccl	WR	27	1	19	17				16	17	2				<1		99
34108	Waikukupa R	5#	WR	27	<1	20	16				13	20	4				<1		100
36962	Robinson Ck	4	WR	40	14	21	4					17	5						101

36961	Robinson Ck	5	WR	32	6	32			19	7	2			3		101
36960	Robinson Ck	8	WR	35	2	41				16	2			5		101
34109	Martyr R	5fol	WR	8	4	15	<1			35	39				<1	101
34958	Martyr R	5	WR	37	4	7	1			36	15					100
34115	Martyr R	5	< 2 μm	2						70	28					100
34111	McKenzie Ck	5	WR	8	1	1	5		61*		11	13				100
34110	Hokuri Ck	4rim	WR	<1			2				5	93				100
34959	Hokuri Ck	5	WR	2			5		74*		3	12	2	2		26
34116	Hokuri Ck	5	< 2 μm						78*			21	1			22

Table 5. Major element geochemistry of DFDP-1A samples from XRF and ICP-AES analysis. All values are in wt. %.

Sample	Hole depth (m)	Lithology	SiO2	TiO2	Al2O3	Fe2O3t	MnO	MgO	CaO	Na2O	K2O	P2O5	Cr2O3	SrO	BaO	LOI	Total
DFDP1	63.6	1	63.0	0.64	15.05	4.80	0.10	1.62	2.87	3.19	2.78	0.16	0.01	0	0.1	4.12	98.46
DFDP2	66.7	2	63.1	0.83	14.85	4.77	0.09	2.48	4.12	3.19	2.76	0.20	0.01	0.1	0.1	4.92	101.46
DFDP3	70.4	3	65.9	0.57	13.75	4.65	0.07	2.34	2.17	1.87	3.69	0.15	0.01	0	0.1	4.20	99.46
DFDP4	74.5	4	61.7	0.88	15.80	6.22	0.10	2.69	2.69	3.15	2.59	0.19	0.01	0	0.1	4.20	100.34
RW_XRF	78	2	67.4	0.65	15.37	4.95	0.07	1.64	1.91	2.57	2.74	0.15	NA	NA	NA	3.05	100.48
RW_XRF	80.5	4	63.4	0.91	14.75	5.36	0.07	3.03	4.01	2.36	2.88	0.19	NA	NA	NA	3.59	100.55
DFDP5	82.7	4	61.1	0.61	12.50	4.89	0.11	3.36	4.7	1.14	3.2	0.17	0.01	0	0	6.94	98.80
RW_XRF	83.7	4	62.5	0.59	13.87	5.05	0.11	3.18	4.84	1.02	3.66	0.15	NA	NA	NA	5.99	100.99
RW_XRF	85.15	4	66.1	0.66	13.99	5.08	0.07	2.92	2.83	0.86	3.45	0.13	NA	NA	NA	4.65	100.78
DFDP6	86.35	4	65.5	0.27	12.80	2.22	0.09	1.24	4.68	2.95	3.84	0.07	0.01	0	0.1	5.38	99.13
RW_XRF	87.54	4	61.4	0.87	15.12	5.73	0.10	3.07	3.63	2.19	3.56	0.18	NA	NA	NA	4.68	100.52
DFDP7	88.4	4	62.2	0.7	13.90	4.70	0.10	3.05	4.93	1.95	3.12	0.19	0.01	0	0	6.59	101.51
DFDP8	89.34	4	61.1	0.83	14.40	5.20	0.09	3.09	4.87	2.45	3.58	0.21	0.01	0.1	0.1	5.95	101.94
RW_XRF	89.8	4	65.5	0.64	14.02	4.77	0.07	2.99	3.34	0.56	3.84	0.15	NA	NA	NA	5.14	100.99
DFDP9	90.32	4	45.0	0.67	11.00	5.52	0.24	4.89	14.8	0.87	2.43	0.19	0.01	0.1	0	15.55	101.21
DFDP10	90.62	5	56.7	0.68	13.10	5.47	0.14	3.35	6.83	0.74	5.52	0.18	0.01	0	0.1	8.64	101.53
DFDP11	91.3	8	70.5	0.56	14.35	4.14	0.06	1.37	1.36	3.32	2.43	0.14	0.01	0	0.1	1.93	100.26

Table 6. Major element geochemistry of DFDP-1B samples from XRF and ICP-AES analysis. All values are in wt. %.

Sample	Hole depth (m)	Lithology	SiO2	TiO2	Al2O3	Fe2O3t	MnO	MgO	CaO	Na2O	K2O	P2O5	Cr2O3	SrO	BaO	LOI	Total
DFDP12	112.04	4	62.7	0.75	15.05	4.43	0.06	2.78	2.87	1.6	4.23	0.2	0.01	0.03	0.06	6.06	100.8
DFDP13	112.12	3	60.8	0.81	14.00	4.31	0.11	2.54	4.2	1.2	4.26	0.21	0.01	0.03	0.05	6.97	99.5
DFDP14	113.05	3	59.8	1.07	13.95	5.98	0.06	3.43	3.36	2.97	2.83	0.29	0.02	0.05	0.09	4.45	98.35
DFDP15	113.81	3	52.7	1.31	15.95	8.80	0.07	4.9	2.79	2.12	2.59	0.31	0.03	0.03	0.04	6.41	98.05
DFDP16	116.72	3	55.1	0.73	13.75	6.61	0.12	4.03	5.24	1.46	2.91	0.22	0.01	0.04	0.04	8.6	98.86
DFDP17	128.04	4	57.3	0.66	12.75	4.45	0.12	3.15	5.42	0.18	3.86	0.15	0.02	0.02	0.03	8.45	96.56
DFDP18	128.09	4	57.7	0.55	12.30	4.69	0.13	2.88	6.36	0.85	3.21	0.15	0.01	0.02	0.02	8.6	97.47
DFDP19	128.22	4	56.3	0.65	12.05	5.06	0.12	3.49	6.72	1.71	2.66	0.18	0.01	0.04	0.04	8.84	97.87
DFDP20	128.3	5	59.2	0.65	12.75	4.89	0.11	2.84	5.32	2.32	2.72	0.18	0.01	0.06	0.07	8.07	99.19
DFDP21	128.5	6	70.7	0.44	15.20	2.92	0.02	1.39	0.58	3.45	4.09	0.15	0.01	0.04	0.08	2.16	101.2
DFDP22	128.53	6	73.6	0.14	13.60	1.31	0.01	0.59	0.46	3.86	4.19	0.1	<0.01	0.03	0.08	1.45	99.42
DFDP23	128.8	6	71.7	0.18	13.45	1.61	0.02	0.69	1.12	3.03	4.43	0.12	<0.01	0.03	0.07	2.12	98.57
DFDP24	128.8	6	70.7	0.19	13.25	1.94	0.02	0.92	0.51	3.83	3.46	0.06	0.01	0.03	0.07	1.95	96.94
DFDP25	130.88	6	63.2	0.88	13.90	6.61	0.08	3.31	2.58	2.01	3.36	0.29	0.03	0.03	0.07	4.84	101.2
DFDP26	131.68	6	74.6	0.1	13.55	0.79	0.01	0.29	1.1	3.29	4.59	0.16	<0.01	0.03	0.07	NSS	NSS
DFDP27	132.7	6	68.1	0.47	14.25	3.71	0.03	1.61	0.97	2.2	3.99	0.19	0.01	0.03	0.07	2.65	98.28
DFDP28	133.75	6	61.4	0.87	15.20	7.01	0.06	3.28	1.28	1.00	3.41	0.17	0.02	0.02	0.06	4.57	98.35
DFDP29	138.17	6	62.7	0.66	16.70	4.62	0.04	2.09	1.28	2.35	4.35	0.26	0.01	0.02	0.06	3.3	98.44
DFDP30	140.96	6	57.3	0.58	16.65	7.48	0.08	3.98	2.37	1.21	4.51	0.14	0.03	0.02	0.06	6.17	100.6
DFDP31	141.07	6	63.7	0.24	18.10	2.61	0.03	1.34	1.40	1.64	7.83	0.25	<0.01	0.02	0.1	3.44	100.7
DFDP32	141.35	6	62.0	0.64	15.10	6.11	0.06	3.36	1.96	1.57	3.61	0.17	0.02	0.02	0.07	5.73	100.4
DFDP33	141.77	6	65.0	0.67	14.05	5.38	0.06	2.93	0.89	1.19	3.93	0.11	0.02	0.02	0.1	3.94	98.29
DFDP34	141.9	6	NSS	NSS	NSS	NSS	NSS	NSS	NSS	NSS	NSS	NSS	NSS	NSS	NSS	4.73	NSS

DFDP35	143.9	6	63.0	0.53	12.55	3.81	0.1	2.10	5.17	1.53	3.03	0.16	0.01	0.02	0.03	7.08	99.12
DFDP36	144.02	5	59.8	0.73	13.95	5.59	0.1	3.40	5.03	1.95	2.43	0.2	0.02	0.08	0.09	8.53	101.9
DFDP37	144.15	5	68.0	0.66	14.95	4.73	0.04	2.46	1.34	2.63	3.41	0.25	0.01	0.04	0.07	3.25	101.8
DFDP38	144.28	7	60.3	0.95	14.80	6.51	0.07	3.37	2.78	1.68	3.52	0.14	0.02	0.03	0.14	3.88	98.19
DFDP39	146.25	7	59.7	1.07	16.35	6.21	0.06	2.55	4.78	3.43	2.31	0.44	0.03	0.09	0.11	1.81	98.94

1260

Table 7. Alteration reactions occurring in Alpine Fault rocks.

Reaction	**ΔV_{solid} (cm^3)**	**ΔV_{solid} (%)**
1. K-feldspar + Na^+ = Albite + K^+	-9	-8
2. 3albite + $2H^+$ + K^+ = muscovite + $6SiO_2$ + $3Na^+$	-23	-8
3. 3K-feldspar + $2H^+$ = muscovite + $6SiO_2$ + $2K^+$	-49	-15
4. 2phlogopite + $4H^+$ + H_2O = clinochlore + $2SiO_2$ + Mg^{2+} + $2K^+$	-25	-8
5. phlogopite + $6H^+$ = K-feldspar + $3Mg^{2+}$ + $4H_2O$	-41	-27
6. 2K-feldspar + $5Mg^{2+}$ + $8H_2O$ = clinochlore + $3SiO_2$ + $2K^+$ + $8H^+$	61	30
7. 3clinochlore + $2K^+$ + $28H^+$ = 2muscovite + $3SiO_2$ + $15Mg^{2+}$ + $24H_2O$	-272	-44
8. 3muscovite + 5biotite + $9SiO_2$ + $4H_2O$ = 8K-feldspar + 3clinochlore	-41	-2.7
9. 2K-feldspar + $6H^+$ = kaolinite + $2K^+$ + $4SiO_2$ + $3H_2O$	-30	-13.7
10. 2albite + $6H^+$ = kaolinite + $2Na^+$ + $4SiO_2$ + $3H_2O$	-12.5	-6.2
11. 5.5muscovite + H^+ = 3illite + K^+ + $3SiO_2$	12.5	6.9
12. clinochlore + 3K-feldspar + H_2O + $9H^+$ = 3montmorillonite + $3Mg^{2+}$ + $3K^+$	41.8	8.1

1261